

Impact of the Dresden-II and COHERENT neutrino scattering data on neutrino electromagnetic properties and electroweak physics

M. Atzori Corona,^{1,2,*} M. Cadeddu,^{2,†} N. Cargioli,^{1,2,‡} F. Dordei,^{2,§}
C. Giunti,^{3,¶} Y.F. Li,^{4,5,**} C. A. Ternes,^{3,††} and Y.Y. Zhang^{4,5,‡‡}

¹*Dipartimento di Fisica, Università degli Studi di Cagliari,
Complesso Universitario di Monserrato - S.P. per Sestu Km 0.700, 09042 Monserrato (Cagliari), Italy*

²*Istituto Nazionale di Fisica Nucleare (INFN), Sezione di Cagliari,
Complesso Universitario di Monserrato - S.P. per Sestu Km 0.700, 09042 Monserrato (Cagliari), Italy*

³*Istituto Nazionale di Fisica Nucleare (INFN),
Sezione di Torino, Via P. Giuria 1, I-10125 Torino, Italy*

⁴*Institute of High Energy Physics, Chinese Academy of Sciences, Beijing 100049, China*

⁵*School of Physical Sciences, University of Chinese Academy of Sciences, Beijing 100049, China
(Dated: Wednesday 15/03/23, 01:01)*

Coherent elastic neutrino-nucleus scattering (CE ν NS) represents a powerful tool to investigate key electroweak physics parameters and neutrino properties since its first observation in 2017 by the COHERENT experiment exploiting the spallation neutron source at Oak Ridge National Laboratory. In light of the recent detection of such a process with antineutrinos produced by the Dresden-II reactor scattering off a germanium detector, we revisit the limits so far set on the neutrino magnetic moments, charge radii and millicharges as well as on the weak mixing angle. In order to do so, we also include the contribution of elastic neutrino-electron scattering, whose effect becomes non negligible in some beyond the Standard Model theories. By using different hypotheses for the germanium quenching factor and the reactor antineutrino flux, we provide a measurement of the weak mixing angle at the low-energy scale of the Dresden-II reactor experiment and, thanks to a combined analysis with the latest cesium iodide and argon data set released by the COHERENT Collaboration, we deliver updated limits for the neutrino electromagnetic properties. Interestingly, we are able to set a new best upper limit on the electron neutrino charge radius and significantly improve the other CE ν NS-related limits on the neutrino electric charge and magnetic moment.

I. INTRODUCTION

Until recently, coherent elastic neutrino-nucleus scattering (CE ν NS) has been observed only exploiting neutrinos coming from the spallation neutron source (SNS) at the Oak Ridge National Laboratory by the COHERENT Collaboration [1]. Indeed, by making use of neutrinos produced by pion-decay-at-rest (π DAR) at the SNS, the CE ν NS process has been observed in 2017 using cesium-iodide (CsI) [1, 2] as well as in argon (Ar) in 2020 [3, 4]. The CsI analysis has also been updated in 2021 with a refined quenching factor (QF) determination and more statistics [5]. The CE ν NS process is a pure neutral current interaction which happens when low energy neutrinos elastically scatter off atomic nuclei with a small momentum transfer between the incoming neutrino and the target nucleus, such that the neutrino interacts coherently with the entire nucleus [6]. When this happens, the cross section becomes roughly proportional to the square of the number of neutrons participating in the interaction. The CE ν NS process proved to be a powerful tool to test new physics interactions beyond the Standard Model (SM) [7–13] as well as to perform stringent tests of nuclear physics, astrophysics, neutrino properties and electroweak interactions [7, 9–12, 14–32].

An alternative source of neutrinos to π DAR are antineutrinos produced at nuclear power reactors. As continuous and well-localized sources, they offer the advantage of very intense fluxes of low-energy antineutrinos ($E < 10$ MeV), with the drawback of a larger background that cannot be removed exploiting the

* mattia.atzori.corona@ca.infn.it

† matteo.cadeddu@ca.infn.it

‡ nicola.cargioli@ca.infn.it

§ francesca.dordei@cern.ch

¶ carlo.giunti@to.infn.it

** liyufeng@ihep.ac.cn

†† ternes@to.infn.it

‡‡ zhangyiyu@ihep.ac.cn

pulsed feature of sources like the SNS. Due to the increased experimental challenge, the CONNIE [33] and CONUS [34, 35] Collaborations have only managed to put stringent limits on $\text{CE}\nu\text{NS}$ observation with reactor antineutrinos. However, recently a tantalizing evidence of $\text{CE}\nu\text{NS}$ using reactor antineutrinos has been reported in Ref. [36] using an ultra-low noise 2.924 kg p-type point-contact germanium detector, called NCC-1701, located 10.39 meters away from the Dresden-II boiling water reactor. The data released corresponds to 96.4 days of effective exposure. Thanks to the much lower energy of reactor antineutrinos and the low energy threshold of such a detector, namely 0.2 keV_{ee}, these data provide complementary information with respect to πDAR sources, with negligible dependence on the neutron distribution inside the target nucleus. This feature makes the bounds extracted using reactor antineutrinos robust against possible variations of the neutron distribution root mean square (rms) radius, that is experimentally poorly known, with the drawback that no information on the latter can be extracted [17].

In this paper, we analyse the new Dresden-II data, revisiting the limits so far set using $\text{CE}\nu\text{NS}$ on the neutrino magnetic moments, charge radii and millicharges as well as on the weak mixing angle. In order to do so, we also perform a combined analysis with the latest CsI and Ar data set released by the COHERENT Collaboration, using different hypotheses for the germanium quenching factor and the reactor antineutrino flux. We will also introduce the contribution of the elastic neutrino-electron scattering, that is observed to be non negligible when some neutrino electromagnetic properties beyond the SM (BSM) are taken into account, namely for the electric charges and magnetic moments, whose contributions are significantly enhanced at low recoil energies.

The paper is organized as follows. In Sec. II, we present the theoretical framework with particular emphasis on the influence of neutrino electromagnetic properties and the weak mixing angle on the $\text{CE}\nu\text{NS}$ cross section and we will discuss the effect of elastic neutrino-electron scattering on the constraints presented in this work. In Sec. III the methods and inputs used for the data analysis are described. In Sec. IV, the combined constraints of the Dresden-II data with the COHERENT CsI and Ar data set are presented. Finally, we draw our conclusions in Sec. V.

II. THEORETICAL FRAMEWORK

In this section, the $\text{CE}\nu\text{NS}$ differential cross section in the SM will be introduced, together with the modifications necessary to include the contribution of possible neutrino charge radii, electric charges and magnetic moments. Moreover, we will also briefly summarize the phenomenology behind the elastic neutrino-electron scattering.

The $\text{CE}\nu\text{NS}$ differential cross section as a function of the nuclear kinetic recoil energy T_{nr} for a neutrino ν_ℓ ($\ell = e, \mu, \tau$) that scatters off a nucleus \mathcal{N} is given by [37–39]

$$\frac{d\sigma_{\nu_\ell\mathcal{N}}}{dT_{\text{nr}}}(E, T_{\text{nr}}) = \frac{G_F^2 M}{\pi} \left(1 - \frac{MT_{\text{nr}}}{2E^2}\right) (Q_{\ell,\text{SM}}^V)^2, \quad (1)$$

where G_F is the Fermi constant, E is the neutrino energy, M the nuclear mass, and

$$Q_{\ell,\text{SM}}^V = [g_V^p(\nu_\ell) Z F_Z(|\vec{q}|^2) + g_V^n N F_N(|\vec{q}|^2)] \quad (2)$$

is the weak charge of the nucleus. Here, Z and N are the numbers of protons and neutrons in the nucleus, respectively. In this analysis, we set $(Z, N)_{\text{Cs}} = (55, 78)$, $(Z, N)_{\text{I}} = (53, 74)$ and $(Z, N)_{\text{Ar}} = (18, 22)$. Actually, one should consider that atmospheric argon is contaminated by a small percentage of ^{36}Ar and ^{38}Ar , namely $f(^{36}\text{Ar}) = 0.33\%$ and $f(^{38}\text{Ar}) = 0.06\%$ [40]. However, since the amount of these contaminants is very small and the uncertainties are large, in practice one gets the same results considering $f(^{40}\text{Ar}) = 100\%$. For Ge we use $(Z, N)_{70, 72, 73, 74, 76\text{Ge}} = (32, (38, 40, 41, 42, 44))$ with the corresponding natural abundances of 0.2057, 0.2745, 0.0775, 0.3650, 0.0773 [41]. The neutrino-proton, g_V^p , and neutrino-neutron, g_V^n , vector couplings correspond to $g_V^p(\nu_e) = 0.0382$, $g_V^p(\nu_\mu) = 0.0300$ and $g_V^n = -0.5117$, when taking into account radiative corrections in the $\overline{\text{MS}}$ scheme [14, 42, 43]. The proton, $F_Z(|\vec{q}|^2)$, and neutron, $F_N(|\vec{q}|^2)$, nuclear form factors represent the Fourier transforms of the corresponding nucleon distribution in the nucleus and

describe the loss of coherence for large values of the momentum transfer $|\vec{q}|$. We use an analytic expression, namely the Helm parameterization [44], for the form factors, that is practically equivalent to the other two well known parameterizations, i.e., the symmetrized Fermi [45] and Klein-Nystrand [46] ones. However, it is important to note that while the form factors are key ingredients in the analysis of COHERENT data, in the energy window of the Dresden-II experiment the form factor of both protons and neutrons is practically equal to unity, making the particular choice of the parameterization completely insignificant. The proton rms radii can be obtained from the muonic atom spectroscopy and electron scattering data [47–49] as explained in Ref. [14], and correspond to

$$R_p(\text{Cs}) = 4.821(5) \text{ fm}, \quad R_p(\text{I}) = 4.766(8) \text{ fm}, \quad R_p(\text{Ar}) = 3.448(2) \text{ fm}, \quad R_p(\text{Ge}) = 4.073(1) \text{ fm}. \quad (3)$$

On the other hand, there is poor knowledge of the values of the ^{133}Cs , ^{127}I , ^{40}Ar , and Ge neutron rms radii using electroweak probes [14, 19–21, 23–25, 50, 51]. The values of these neutron rms radii can, however, be estimated with theoretical calculations based on different nuclear models [14, 17, 52]. Here, we consider the following values obtained from the recent nuclear shell model estimate of the corresponding neutron skins (i.e. the differences between the neutron and the proton rms radii) in Ref. [52]

$$R_n(^{133}\text{Cs}) \simeq 5.09 \text{ fm}, \quad R_n(^{127}\text{I}) \simeq 5.03 \text{ fm}, \quad R_n(^{40}\text{Ar}) \simeq 3.55 \text{ fm}, \quad R_n(\text{Ge}) \simeq 4.15\text{--}4.28 \text{ fm}, \quad (4)$$

where for Ge a neutron skin of 0.08–0.17 fm has been considered [52]. Concerning the COHERENT data [3–5], we take into account the effect of the uncertainty of the values of the neutron rms radii by considering 3.4% and 2% uncertainties for the CsI and Ar CE ν NS rates, respectively.

A. Neutrino-electron elastic scattering

Neutrino-electron elastic scattering (ES) is a concurrent process to CE ν NS. In the SM, its contribution to the total event rate at low recoil energies is very small and thus it is usually neglected in CE ν NS analyses. However, in certain BSM scenarios the ES contribution could increase significantly, making it important to include it since stronger constraints can be obtained [53]. For the Ar data set, the COHERENT Collaboration performed a selection exploiting the so-called f_{90} parameter [3, 4], namely the ratio between the integrated photomultiplier amplitude in the first 90 ns with respect to the total amplitude. This parameter permits to perform strong pulse shape discrimination between nuclear recoils due to CE ν NS and electron recoils due to ES, such that the latter contribution becomes completely negligible. However, there is no similar feature that can be exploited in the COHERENT CsI data set, nor in the Dresden-II one, making it important to fit also for the ES contribution.

The SM neutrino-electron elastic scattering cross section per atom \mathcal{A} is obtained multiplying the ES cross section per electron with the effective electron charge of the target atom $Z_{\text{eff}}^{\mathcal{A}}(T_e)$ [53], namely

$$\frac{d\sigma_{\nu_e-\mathcal{A}}^{\text{ES}}}{dT_e}(E, T_e) = Z_{\text{eff}}^{\mathcal{A}}(T_e) \frac{G_F^2 m_e}{2\pi} \left[(g_V^{\nu_e} + g_A^{\nu_e})^2 + (g_V^{\nu_e} - g_A^{\nu_e})^2 \left(1 - \frac{T_e}{E}\right)^2 - ((g_V^{\nu_e})^2 - (g_A^{\nu_e})^2) \frac{m_e T_e}{E^2} \right], \quad (5)$$

where m_e is the electron mass, T_e is the electron recoil energy, and the neutrino-flavour dependent electron couplings are

$$g_V^{\nu_e} = 2 \sin^2 \theta_W + 1/2, \quad g_A^{\nu_e} = 1/2, \quad (6)$$

$$g_V^{\nu_{\mu,\tau}} = 2 \sin^2 \theta_W - 1/2, \quad g_A^{\nu_{\mu,\tau}} = -1/2. \quad (7)$$

For antineutrinos one must substitute $g_A \rightarrow -g_A$. Here, θ_W is the weak mixing angle, also known as the Weinberg angle, whose value at zero momentum transfer is $\sin^2 \theta_W = 0.23857$ [43] in the $\overline{\text{MS}}$ scheme. The $Z_{\text{eff}}^{\mathcal{A}}(T_e)$ term [54, 55] quantifies the number of electrons that can be ionized by a certain energy deposit T_e . It is needed to correct the cross section derived under the Free Electron Approximation (FEA) hypothesis, where electrons are considered to be free and at rest [56–59]. It is given for Cs, I and Ge in Tabs. I and II [60], respectively. In the sub-keV regime, as in the case of Dresden-II, energies are comparable with those of

atomic scales and a correction to the FEA analogous to the $Z_{\text{eff}}^A(T_e)$ term is mandatory. An alternative approach, that takes into account the many-electron dynamics in atomic ionization is obtained by exploiting an ab-initio approach in the framework of the multi-configuration relativistic random phase approximation (MCRPRA) [61–63], which is able to give an improved description of the atomic many-body effects. On the other hand, FEA, in particular when corrected by the stepping function $Z_{\text{eff}}^A(T_e)$, is known to provide a very good approximation at higher energies, as in the case of COHERENT CsI. Throughout this paper, we will discuss the validity of our results concerning this issue.

$Z_{\text{eff}}^{\text{Cs}} =$	55, $T_e > 35.99 \text{ keV}$	$Z_{\text{eff}}^{\text{I}} =$	53, $T_e > 33.17 \text{ keV}$
	53, $35.99 \text{ keV} \geq T_e > 5.71 \text{ keV}$		51, $33.17 \text{ keV} \geq T_e > 5.19 \text{ keV}$
	51, $5.71 \text{ keV} \geq T_e > 5.36 \text{ keV}$		49, $5.19 \text{ keV} \geq T_e > 4.86 \text{ keV}$
	49, $5.36 \text{ keV} \geq T_e > 5.01 \text{ keV}$		47, $4.86 \text{ keV} \geq T_e > 4.56 \text{ keV}$
	45, $5.01 \text{ keV} \geq T_e > 1.21 \text{ keV}$		43, $4.56 \text{ keV} \geq T_e > 1.07 \text{ keV}$
	43, $1.21 \text{ keV} \geq T_e > 1.07 \text{ keV}$		41, $1.07 \text{ keV} \geq T_e > 0.93 \text{ keV}$
	41, $1.07 \text{ keV} \geq T_e > 1 \text{ keV}$		39, $0.93 \text{ keV} \geq T_e > 0.88 \text{ keV}$
	37, $1 \text{ keV} \geq T_e > 0.74 \text{ keV}$		35, $0.88 \text{ keV} \geq T_e > 0.63 \text{ keV}$
	33, $0.74 \text{ keV} \geq T_e > 0.73 \text{ keV}$		31, $0.63 \text{ keV} \geq T_e > 0.62 \text{ keV}$
	27, $0.73 \text{ keV} \geq T_e > 0.23 \text{ keV}$		25, $0.62 \text{ keV} \geq T_e > 0.19 \text{ keV}$
	25, $0.23 \text{ keV} \geq T_e > 0.17 \text{ keV}$		23, $0.19 \text{ keV} \geq T_e > 0.124 \text{ keV}$
	23, $0.17 \text{ keV} \geq T_e > 0.16 \text{ keV}$		21, $0.124 \text{ keV} \geq T_e > 0.123 \text{ keV}$
	19, $T_e < 0.16 \text{ keV}$		17, $T_e < 0.123 \text{ keV}$

TABLE I. The effective electron charge of the target atom, $Z_{\text{eff}}^A(T_e)$, for Cs and I.

$Z_{\text{eff}}^{\text{Ge}} =$	32, $T_e > 11.103 \text{ keV}$
	30, $11.103 \text{ keV} \geq T_e > 1.4146 \text{ keV}$
	28, $1.4146 \text{ keV} \geq T_e > 1.2481 \text{ keV}$
	26, $1.2481 \text{ keV} \geq T_e > 1.217 \text{ keV}$
	22, $1.217 \text{ keV} \geq T_e > 0.1801 \text{ keV}$
	20, $0.1801 \text{ keV} \geq T_e > 0.1249 \text{ keV}$
	18, $0.1249 \text{ keV} \geq T_e > 0.1208 \text{ keV}$
	14, $0.1208 \text{ keV} \geq T_e > 0.0298 \text{ keV}$
	10, $0.0298 \text{ keV} \geq T_e > 0.0292 \text{ keV}$
	4, $T_e \leq 0.0292 \text{ keV}$

TABLE II. The effective electron charge of the target atom, $Z_{\text{eff}}^A(T_e)$, for Ge.

B. Neutrino charge radii

In the SM, the neutrino charge radii (CR) are the only electromagnetic properties of neutrinos that are different from zero. The contribution of the SM neutrino CR is taken into account as one of the radiative

corrections to $g_V^p(\nu_\ell)$ and corresponds to [64–66]

$$\langle r_{\nu_\ell}^2 \rangle_{\text{SM}} = -\frac{G_F}{2\sqrt{2}\pi^2} \left[3 - 2 \ln \left(\frac{m_\ell^2}{m_W^2} \right) \right], \quad (8)$$

where m_W and m_ℓ are the W boson and charged lepton masses ($\ell = e, \mu, \tau$) respectively, and we use the conventions in Refs. [21, 23, 67]. The SM neutrino CR are diagonal in the flavor basis, due to the conservation of generation lepton numbers. Numerically, the predicted values of $\langle r_{\nu_e}^2 \rangle_{\text{SM}}$ and $\langle r_{\nu_\mu}^2 \rangle_{\text{SM}}$, that can be probed with CE ν NS data, are

$$\langle r_{\nu_e}^2 \rangle_{\text{SM}} = -0.83 \times 10^{-32} \text{ cm}^2, \quad (9)$$

$$\langle r_{\nu_\mu}^2 \rangle_{\text{SM}} = -0.48 \times 10^{-32} \text{ cm}^2. \quad (10)$$

Here, we want to constrain possible BSM effects that could modify the SM value of the neutrino CR. Thus, we consider the general case in which neutrinos can have both diagonal and off-diagonal, also referred to as transition, CR in the flavor basis that can be generated by BSM physics. The differential CE ν NS cross section that takes into account the contribution of the neutrino charge radii in addition to the SM neutral-current weak interaction is

$$\frac{d\sigma_{\nu_\ell \mathcal{N}}^{\text{CR}}(E, T_{\text{nr}})}{dT_{\text{nr}}} = \frac{G_F^2 M}{\pi} \left(1 - \frac{MT_{\text{nr}}}{2E^2} \right) \left\{ \left[(\tilde{g}_V^p - \tilde{Q}_{\ell\ell}) ZF_Z(|\vec{q}|^2) + g_V^n NF_N(|\vec{q}|^2) \right]^2 + Z^2 F_Z^2(|\vec{q}|^2) \sum_{\ell' \neq \ell} |\tilde{Q}_{\ell\ell'}|^2 \right\}, \quad (11)$$

where $\tilde{g}_V^p = 0.0186$ is the neutrino-proton coupling without the contribution of the SM neutrino CR. The effects of the charge radii $\langle r_{\nu_{\ell\ell'}}^2 \rangle$ in the cross section are expressed as [57]

$$\tilde{Q}_{\ell\ell'} = \frac{\sqrt{2}\pi\alpha}{3G_F} \langle r_{\nu_{\ell\ell'}}^2 \rangle, \quad (12)$$

where α is the electromagnetic fine-structure constant. The diagonal CR of flavor neutrinos contribute to the cross section coherently with the neutrino-proton neutral current interaction, generating an effective shift of $\sin^2\vartheta_W$. In the case of $\bar{\nu}_\ell \mathcal{N}$ scattering, we have $g_V^{p,n} \rightarrow -g_V^{p,n}$ and $\langle r_{\nu_{\ell\ell'}} \rangle \rightarrow \langle r_{\bar{\nu}_{\ell\ell'}} \rangle = -\langle r_{\nu_{\ell\ell'}} \rangle$. Therefore, the CR of flavor neutrinos and antineutrinos contribute with the same sign to the shift of $\sin^2\vartheta_W$ in the CE ν NS cross section.

There are five CR that can be determined with the CE ν NS data: the two diagonal charge radii $\langle r_{\nu_{ee}}^2 \rangle$ and $\langle r_{\nu_{\mu\mu}}^2 \rangle$, that sometimes are denoted with the simpler notation $\langle r_{\nu_e}^2 \rangle$ and $\langle r_{\nu_\mu}^2 \rangle$ in connection to the SM CR in Eqs. (8)–(10), and the absolute values of the three off-diagonal CR $\langle r_{\nu_{e\mu}}^2 \rangle = \langle r_{\nu_{\mu e}}^2 \rangle^*$, $\langle r_{\nu_{e\tau}}^2 \rangle$, and $\langle r_{\nu_{\mu\tau}}^2 \rangle$.

In the presence of the neutrino charge radii, the neutrino-electron elastic scattering cross section in Eq. (5), is modified to [57]

$$\left(\frac{d\sigma_{\nu_\ell \mathcal{A}}^{\text{ES,CR}}}{dT_e} \right)_{\text{SM}+\tilde{Q}} = \left(\frac{d\sigma_{\nu_\ell \mathcal{A}}^{\text{ES,CR}}}{dT_e} \right)_{\text{SM}+\tilde{Q}_{\ell\ell}} + \sum_{\ell' \neq \ell} \left(\frac{d\sigma_{\nu_\ell \mathcal{A}}^{\text{ES,CR}}}{dT_e} \right)_{\tilde{Q}_{\ell\ell'}}, \quad (13)$$

where $(d\sigma_{\nu_\ell \mathcal{A}}^{\text{ES,CR}}/dT_e)_{\text{SM}+\tilde{Q}_{\ell\ell}}$ is given by Eq. (5) with

$$g_V^{\nu_\ell} \rightarrow g_V^{\nu_\ell} + \tilde{Q}_{\ell\ell}, \quad (14)$$

and

$$\left(\frac{d\sigma_{\nu_\ell \mathcal{A}}^{\text{ES,CR}}}{dT_e} \right)_{\tilde{Q}_{\ell\ell'}} = Z_{\text{eff}}^{\mathcal{A}}(T_e) \frac{\pi\alpha^2 m_e}{9} \left[1 + \left(1 - \frac{T_e}{E} \right)^2 - \frac{m_e T_e}{E^2} \right] |\langle r_{\nu_{\ell\ell'}}^2 \rangle|^2, \quad (15)$$

for $\ell' \neq \ell$. In this scenario, the FEA approach corrected by the stepping function as used in this work slightly overestimates the cross section with respect to MCRRPA for $T_e \lesssim 1$ keV, but they rapidly converge for $T_e > 1$ keV [58], causing a negligible difference.

C. Neutrino magnetic moments

The neutrino magnetic moment (MM) is the most investigated neutrino electromagnetic property, both theoretically and experimentally. Indeed, its existence is predicted by many BSM theories, especially those that include right-handed neutrinos, see the reviews in Refs. [67, 68]. The differential CE ν NS cross section that takes into account the contribution of the neutrino magnetic moment is given by adding to the SM cross section in Eq. (1) the MM contribution, namely

$$\frac{d\sigma_{\nu_\ell-\mathcal{N}}^{\text{MM}}}{dT_{\text{nr}}}(E, T_{\text{nr}}) = \frac{\pi\alpha^2}{m_e^2} \left(\frac{1}{T_{\text{nr}}} - \frac{1}{E} \right) Z^2 F_Z^2(|\vec{q}|^2) \left| \frac{\mu_{\nu_\ell}}{\mu_B} \right|^2, \quad (16)$$

where μ_{ν_ℓ} is the effective MM of the flavor neutrino ν_ℓ in elastic scattering (see Ref. [67]), and μ_B is the Bohr magneton.

In the case of neutrino-electron scattering, the cross section in presence of neutrino magnetic moments receives an additional contribution equal to

$$\frac{d\sigma_{\nu_\ell-\mathcal{A}}^{\text{ES, MM}}}{dT_e}(E, T_e) = Z_{\text{eff}}^{\mathcal{A}}(T_e) \frac{\pi\alpha^2}{m_e^2} \left(\frac{1}{T_e} - \frac{1}{E} \right) \left| \frac{\mu_{\nu_\ell}}{\mu_B} \right|^2, \quad (17)$$

with $Z_{\text{eff}}^{\mathcal{A}}(T_e)$ detailed in Tabs. I and II. As in the case of neutrino charge radii, the cross section obtained with the corrected FEA is slightly larger than the MCRPRA one only for $T_e \lesssim 1$ keV [58].

D. Neutrino electric charges

As already shown in many experimental and theoretical studies (for a review see Ref. [67]), CE ν NS process is sensitive not only to the neutrino CR, but also to the existence of neutrino electric charges (EC). Indeed, even if neutrinos are considered as neutral particles, in some BSM theories they can acquire small electric charges, usually referred to as millicharges. The differential CE ν NS cross section taking into account the contribution of the neutrino electric charges in addition to SM neutral-current weak interactions is similar to that derived for the neutrino charge radii, with g_V^p and g_V^n given in Sec. II and $\tilde{Q}_{\ell\ell'}$ replaced by $Q_{\ell\ell'}$ [57, 67]

$$Q_{\ell\ell'} = \frac{2\sqrt{2}\pi\alpha}{G_F q^2} q_{\nu_{\ell\ell'}}, \quad (18)$$

where $q_{\nu_{\ell\ell'}}$ is the neutrino EC and $q^2 = -2MT_{\text{nr}}$ is the squared four-momentum transfer. Given the extremely low momentum transfer and low-energy thresholds of reactor experiments, the q^2 dependence in the denominator of Eq. (18) helps to set more stringent constraints using the data of Dresden-II with respect to COHERENT, as we will show in Sec. IV. As in the case of neutrino CR, the contribution of neutrinos and antineutrinos to the neutrino EC will also shift $\sin^2\vartheta_W$ with the same sign, since the electric charges of neutrino and antineutrino are opposite as well as the weak neutral current couplings.

If neutrinos have electric charges, the neutrino-electron elastic scattering cross section in Eq. (5) becomes [57]

$$\left(\frac{d\sigma_{\nu_\ell-\mathcal{A}}^{\text{ES, EC}}}{dT_e} \right)_{\text{SM}+Q} = \left(\frac{d\sigma_{\nu_\ell-\mathcal{A}}^{\text{ES, EC}}}{dT_e} \right)_{\text{SM}+Q_{\ell\ell}} + \sum_{\ell' \neq \ell} \left(\frac{d\sigma_{\nu_\ell-\mathcal{A}}^{\text{ES, EC}}}{dT_e} \right)_{Q_{\ell\ell'}}, \quad (19)$$

where $(d\sigma_{\nu_\ell-\mathcal{A}}^{\text{ES, EC}}/dT_e)_{\text{SM}+Q_{\ell\ell}}$ is given by Eq. (5) with

$$g_V^{\nu_\ell} \rightarrow g_V^{\nu_\ell} + Q_{\ell\ell}, \quad (20)$$

and

$$\left(\frac{d\sigma_{\nu_\ell-\mathcal{A}}^{\text{ES, EC}}}{dT_e} \right)_{Q_{\ell\ell'}} = Z_{\text{eff}}^{\mathcal{A}}(T_e) \frac{\pi\alpha^2}{m_e T_e^2} \left[1 + \left(1 - \frac{T_e}{E} \right)^2 - \frac{m_e T_e}{E^2} \right] |q_{\nu_{\ell\ell'}}|^2, \quad (21)$$

for $\ell' \neq \ell$. In neutrino-electron elastic scattering $|q^2| = 2m_e T_e$, which is much smaller than the CE ν NS $|q^2|$. Therefore, the analysis of the COHERENT CsI and Dresden-II data taking into account ES scattering allows us to enhance substantially the sensitivity to neutrino millicharges. Let us note that, for neutrino millicharges, the MCRPRA cross section for $T_e \lesssim 1$ keV is more than one order of magnitude bigger than that obtained with the corrected FEA [58]. In this respect, we can consider our Dresden-II ES limits as conservative and tighter limits are expected if the MCRPRA approach is used.

III. DATA ANALYSIS STRATEGY

In this section we will summarize the prescriptions followed for the analysis of the COHERENT and Dresden-II data set.

A. COHERENT

For the analysis of the COHERENT CsI and Ar data we follow closely the strategy explained in detail in Ref. [69]. We obtained information on all the quantities used from Refs. [3, 4] for the Ar data and from Ref. [5] for the CsI data. The total differential neutrino flux, dN_ν/dE , is given by the sum of the three neutrino components produced by the pion decay at rest. Namely, the first prompt component is coming directly from the pion decay ($\pi^+ \rightarrow \mu^+ + \nu_\mu$), while the second two delayed components are coming from the subsequent muon decay ($\mu^+ \rightarrow e^+ + \nu_e + \bar{\nu}_\mu$). The neutrino flux depends on the number r of neutrinos produced for each proton-on-target (POT), the number of protons-on-target N_{POT} and the baseline L between the source and the detector. For the COHERENT Ar detector, called CENNS-10, we use $r = 0.09$, $N_{\text{POT}} = 13.8 \times 10^{22}$ and $L = 27.5$ m [4]. For the COHERENT CsI detector, we use $r = 0.0848$, $N_{\text{POT}} = 3.198 \times 10^{23}$ and $L = 19.3$ m [2]. The prompt ν_μ 's component arrives within about 1 μ s from the on-beam trigger, whereas the delayed ν_e 's and $\bar{\nu}_\mu$'s arrive in a time interval which can extend up to about 10 μ s. The inclusion of the time evolution of the COHERENT data is thus important to distinguish the two neutrino components.

In each nuclear-recoil energy-bin i , the theoretical CE ν NS event number $N_i^{\text{CE}\nu\text{NS}}$ is given by

$$N_i^{\text{CE}\nu\text{NS}}(\mathcal{N}) = N(\text{tg}) \int_{T_{\text{nr}}^i}^{T_{\text{nr}}^{i+1}} dT_{\text{nr}} A(T_{\text{nr}}) \int_0^{T_{\text{nr}}'^{\text{max}}} dT_{\text{nr}}' R(T_{\text{nr}}, T_{\text{nr}}') \int_{E_{\text{min}}(T_{\text{nr}}')}^{E_{\text{max}}} dE \sum_{\nu=\nu_e, \nu_\mu, \bar{\nu}_\mu} \frac{dN_\nu}{dE}(E) \frac{d\sigma_{\nu-\mathcal{N}}}{dT_{\text{nr}}'}(E, T_{\text{nr}}'), \quad (22)$$

where $\mathcal{N} = \text{Cs, I or Ar}$, and $N_i^{\text{CE}\nu\text{NS}}(\text{CsI}) = N_i^{\text{CE}\nu\text{NS}}(\text{Cs}) + N_i^{\text{CE}\nu\text{NS}}(\text{I})$. Moreover, T_{nr} is the reconstructed nuclear recoil kinetic energy, T_{nr}' is the true nuclear recoil kinetic energy, $A(T_{\text{nr}})$ is the energy-dependent detector efficiency, $R(T_{\text{nr}}, T_{\text{nr}}')$ is the energy resolution function, $T_{\text{nr}}'^{\text{max}} \simeq 2E_{\text{max}}^2/M$, $E_{\text{max}} = m_\mu/2 \sim 52.8$ MeV, $E_{\text{min}}(T_{\text{nr}}') \simeq \sqrt{MT_{\text{nr}}'/2}$, m_μ being the muon mass, and $N(\text{tg})$ the number of target atoms in the detector, where the targets are tg = CsI or Ar. The number of target atoms in each detector is given by $N(\text{tg}) = N_A M_{\text{det}}/M_{\text{tg}}$, where N_A is the Avogadro number, M_{det} is the detector active mass ($M_{\text{det}} = 24.4$ kg for Ar and $M_{\text{det}} = 14.6$ kg for CsI), and M_{tg} is the molar mass ($M_{\text{Ar}} = 39.96$ g/mol and $M_{\text{CsI}} = 259.8$ g/mol). Finally, the differential CE ν NS cross section $d\sigma_{\nu-\mathcal{N}}/dT_{\text{nr}}$ has been discussed in Section II.

Differently from Ref. [69], in the CsI analysis we also include the contribution of the electron-neutrino scattering, as stated in Sec. II. In each electron-recoil energy-bin i , the theoretical ES event number N_i^{ES} is given by

$$N_i^{\text{ES}}(\mathcal{A}) = N(\text{tg}) \int_{T_e^i}^{T_e^{i+1}} dT_e A(T_e) \int_0^{T_e'^{\text{max}}} dT_e' R(T_e, T_e') \int_{E_{\text{min}}(T_e')}^{E_{\text{max}}} dE \sum_{\nu=\nu_e, \nu_\mu, \bar{\nu}_\mu} \frac{dN_\nu}{dE}(E) \frac{d\sigma_{\nu-\mathcal{A}}^{\text{ES}}}{dT_e'}(E, T_e'), \quad (23)$$

where $\mathcal{A} = \text{Cs or I}$, and $N_i^{\text{ES}}(\text{CsI}) = N_i^{\text{ES}}(\text{Cs}) + N_i^{\text{ES}}(\text{I})$, $E_{\text{min}}(T_e') = (T_e' + \sqrt{T_e'^2 + 2m_e T_e'})/2$, and $T_e'^{\text{max}} = 2E_{\text{max}}^2/(2E_{\text{max}} + m_e)$.

It is important to consider that the energy actually observed in the detector is the electron-equivalent recoil energy T_e , which is transformed into the nuclear recoil energy T_{nr} in the CE ν NS rate by inverting the

relation

$$T_e = f_Q (T_{nr}) T_{nr}, \quad (24)$$

where f_Q is the quenching factor [70].

In order to include also the timing information we separated the theoretical CE ν NS event numbers $N_i^{\text{CE}\nu\text{NS}}$ in Eq. (22) in time bins that are calculated from the exponential decay laws of the generating pions and muons. With this procedure we obtained the theoretical CE ν NS event numbers $N_{ij}^{\text{CE}\nu\text{NS}}$, where i is the index of the energy bins and j is the index of the time bins.

We performed the analysis of the COHERENT CsI data using the Poissonian least-squares function [43, 71], given that in some energy-time bins the number of events is very small, namely

$$\begin{aligned} \chi_{\text{CsI,CE}\nu\text{NS+ES}}^2 = & 2 \sum_{i=1}^9 \sum_{j=1}^{11} \left[\sum_{z=1}^4 [(1 + \eta_z) N_{ij}^z] + \eta_5 N_{ij}^5 - N_{ij}^{\text{exp}} + N_{ij}^{\text{exp}} \ln \left(\frac{N_{ij}^{\text{exp}}}{\sum_{z=1}^4 [(1 + \eta_z) N_{ij}^z] + \eta_5 N_{ij}^5} \right) \right] \\ & + \sum_{z=1}^5 \left(\frac{\eta_z}{\sigma_z} \right)^2, \end{aligned} \quad (25)$$

where the indices $z = 1, 2, 3, 4, 5$ for N_{ij}^z stand, respectively, for CE ν NS+ES, namely $N_{ij}^1 = N_{ij}^{\text{CE}\nu\text{NS}} + N_{ij}^{\text{ES}}$, beam-related neutron ($N_{ij}^2 = N_{ij}^{\text{BRN}}$), neutrino-induced neutron ($N_{ij}^3 = N_{ij}^{\text{NIN}}$), steady-state ($N_{ij}^4 = N_{ij}^{\text{SS}}$) backgrounds, and CE ν NS only ($N_{ij}^5 = N_{ij}^{\text{CE}\nu\text{NS}}$). In our notation, N_{ij}^{exp} is the experimental event number obtained from coincidence (C) data, $N_{ij}^{\text{CE}\nu\text{NS}}$ is the predicted number of CE ν NS events that depends on the physics model under consideration, N_{ij}^{BRN} is the estimated BRN background, N_{ij}^{NIN} is the estimated NIN background, N_{ij}^{SS} is the SS background obtained from the anti-coincidence (AC) data and, N_{ij}^{ES} is the contribution of the electron scattering that also depends on the physics model under consideration. Clearly, when summing the CE ν NS and ES contributions, both event numbers as well as the background contributions must be determined either in nuclear-recoil or in electron-recoil energy bins. We took into account the systematic uncertainties with the nuisance parameters η_z and the corresponding uncertainties $\sigma_{\text{CE}\nu\text{NS+ES}} = 0.11$, $\sigma_{\text{CE}\nu\text{NS}} = 0.05$, $\sigma_{\text{BRN}} = 0.25$, $\sigma_{\text{NIN}} = 0.35$, $\sigma_{\text{SS}} = 0.021$. The uncertainty $\sigma_{\text{CE}\nu\text{NS+ES}}$ does not include the form factor and quenching factor related uncertainties that are affecting only CE ν NS and are implemented thanks to an additional contribution $\sigma_{\text{CE}\nu\text{NS}}$.

In this work, to appreciate the impact of the ES contribution, we will sometimes fit the CsI data set for CE ν NS only. In this case, the least-squares function $\chi_{\text{CsI,CE}\nu\text{NS}}^2$ is obtained removing the ES contribution for $z = 1$ in Eq. (25).

We performed the analysis of the COHERENT Ar data using the least-squares function

$$\chi_{\text{Ar,CE}\nu\text{NS}}^2 = \sum_{i=1}^{12} \sum_{j=1}^{10} \left(\frac{N_{ij}^{\text{exp}} - \sum_{z=1}^4 (1 + \eta_z + \sum_l \eta_{zl}^{\text{sys}}) N_{ij}^z}{\sigma_{ij}} \right)^2 + \sum_{z=1}^4 \left(\frac{\eta_z}{\sigma_z} \right)^2 + \sum_{z,l} (\epsilon_{zl})^2, \quad (26)$$

where $z = 1, 2, 3, 4$ stands for the theoretical prediction of CE ν NS, SS, Prompt Beam-Related Neutron (PBRN) and Delayed Beam-Related Neutron (DBRN) backgrounds, and N_{ij}^{exp} is the number of observed events in each energy and time bin. The statistical uncertainty σ_{ij} is given by

$$(\sigma_{ij})^2 = (\sigma_{ij}^{\text{exp}})^2 + (\sigma_{ij}^{\text{SS}})^2, \quad (27)$$

where $\sigma_{ij}^{\text{exp}} = \sqrt{N_{ij}^{\text{exp}}}$ and $\sigma_{ij}^{\text{SS}} = \sqrt{N_{ij}^{\text{SS}}/5}$. The factor 1/5 is due to the 5 times longer sampling time of the SS background with respect to the signal time window. The nuisance parameters η_z quantify the systematic uncertainties of the event rate for the theoretical prediction of CE ν NS, SS, PBRN, and DBRN backgrounds, with the corresponding uncertainties $\sigma_{\text{CE}\nu\text{NS}} = 0.13$, $\sigma_{\text{PBRN}} = 0.32$, $\sigma_{\text{DBRN}} = 1$, and $\sigma_{\text{SS}} = 0.0079$. We considered also the systematic uncertainties of the shapes of CE ν NS and PBRN spectra using the information

in the COHERENT data release [4]. This is done in Eq. (26) through the nuisance parameters ϵ_{zl} and the terms $\eta_{zl,ij}^{\text{sys}}$ given by

$$\eta_{zl,ij}^{\text{sys}} = \epsilon_{zl} \frac{N_{zl,ij}^{\text{sys}} - N_{zl,ij}^{\text{CV}}}{N_{zl,ij}^{\text{CV}}}, \quad (28)$$

where l is the index of the source of the systematic uncertainty. Here, $N_{zl,ij}^{\text{sys}}$ and $N_{zl,ij}^{\text{CV}}$ are, respectively, 1σ probability distribution functions (PDFs) described in Tab. 3 of Ref. [4] and the central-value (CV) SM predictions described in Tab. 2 of Ref. [4].

B. Dresden-II

For the analysis of the NCC-1701 data obtained using antineutrinos produced by the Dresden-II reactor, we use the data release and related information in Ref. [36].

In order to derive the antineutrino spectra $dN_{\bar{\nu}}/dE$ from the Dresden-II reactor we have considered three different parametrizations, obtained by combining four different predictions for specific energy ranges. In particular, the neutrino spectra are built by combining the expected spectra for antineutrino energies above 2 MeV from either Ref. [72] or Ref. [73], that we indicate as HM and EF, respectively, with the low energy part determined by Ref. [74] and Refs. [75, 76], that we indicate as VE and K, respectively. In this way, three different combinations are obtained, to which we will refer to as HMVE, EFK, and HMK. These spectra are obtained from the weighted average of the antineutrino fluxes from four main fission isotopes, namely ^{235}U , ^{239}Pu , ^{238}U and ^{241}Pu . In the K prediction [75, 76], the contribution at low energies from radiative neutron capture on ^{238}U is also taken into account. The latter has the effect to enhance the spectrum for neutrino energies below ~ 1 MeV. In all cases, we set the spectra to zero above 10 MeV. The neutrino spectra for reactor antineutrinos have been normalized to the antineutrino flux estimate reported in Ref. [36] and corresponding to $\Phi_{\text{est}} = 4.8 \times 10^{13} \text{ cm}^{-2}\text{s}^{-1}$, that has been determined considering a reactor power $P = 2.96 \text{ GW}_{\text{th}}$ and a reactor-detector distance of $L = 10.39 \text{ m}$ [36].

In the energy region of interest of Dresden-II, $0.2 \text{ keV}_{\text{ee}} < T_e < 1.5 \text{ keV}_{\text{ee}}$, the background comes from the elastic scattering of epithermal neutrons and the electron capture in ^{71}Ge . The epithermal neutron contribution, which is the dominant one in the CE ν NS recoil-energy region, $T_e \lesssim 0.5 \text{ keV}_{\text{ee}}$, is described by an exponential function with decay constant T_{epith} plus a constant term N_{epith} , while the electron capture peaks from ^{71}Ge , namely the L1-, L2- and M-shell peaks, are described each by a Gaussian function. The latter is parametrized by an amplitude A_i , the centroid T_i and the standard deviation σ_i , where $i = \text{L1, L2 and M}$. Thus, the expected event rate of background is given by

$$\frac{dN^{\text{bkg}}}{dT_e} = N_{\text{epith}} + A_{\text{epith}} e^{-T_e/T_{\text{epith}}} + \sum_{i=\text{L1,L2,M}} \frac{A_i}{\sqrt{2\pi}\sigma_i} e^{-\frac{(T_e - T_i)^2}{2\sigma_i^2}}. \quad (29)$$

Following Ref. [36], the total amount of free parameters for the background prediction reduces to: N_{epith} , A_{epith} , T_{epith} , A_{L1} , E_{L1} , σ_{L1} and $\beta_{\text{M/L1}}$. In fact, the amplitude of the L2 shell contribution can be expressed in terms of the amplitude of the L1 shell (A_{L1}), in particular $A_{\text{L2}}/A_{\text{L1}} = 0.008$, and $\sigma_{\text{L2}} = \sigma_{\text{L1}}$. The centroid of the L2 Gaussian can be safely set to the nominal value $T_{\text{L2}} = 1.142 \text{ keV}$. The standard deviation of the M-shell contribution can be fixed to the electronic noise uncertainty, which is $\sigma_n = 68.5 \text{ eV}$ for the Rx-ON (reactor operation period) data. The centroid of the M-shell Gaussian is fixed to its nominal value $T_{\text{M}} = 0.158 \text{ keV}$, being smaller than the experimental threshold whereas its amplitude is left free to vary in the fit with a constraint corresponding to the experimentally determined ratio $\beta_{\text{M/L1}} = A_{\text{M}}/A_{\text{L1}} = 0.16 \pm 0.03$.

The theoretical CE ν NS event-number $N_i^{\text{CE}\nu\text{NS}}$ in each electron-recoil energy-bin i is given by

$$N_i^{\text{CE}\nu\text{NS}}(\mathcal{N}) = N(\text{Ge}) \int_{T_e^i}^{T_e^{i+1}} dT_e \int_{T_{\text{nr}}'^{\text{min}}}^{T_{\text{nr}}'^{\text{max}}} dT_{\text{nr}}' R(T_e, T_e'(T_{\text{nr}}')) \int_{E_{\text{min}}(T_{\text{nr}}')}^{E_{\text{max}}} dE \frac{dN_{\bar{\nu}}}{dE}(E) \frac{d\sigma_{\bar{\nu}-\mathcal{N}}}{dT_{\text{nr}}'}(E, T_{\text{nr}}'), \quad (30)$$

where $\mathcal{N} = \frac{A}{Z}\text{Ge}$ with $A = 70, 72, 73, 74, 76$, and $N_i^{\text{CE}\nu\text{NS}}(\text{Ge}) = \sum_A f_{\frac{A}{Z}\text{Ge}} N_i^{\text{CE}\nu\text{NS}}(\frac{A}{Z}\text{Ge})$, where $f_{\frac{A}{Z}\text{Ge}}$ are the isotopic abundances introduced in Sec. II. Moreover, $N(\text{Ge}) = 2.43 \times 10^{25}$ is the number of germanium

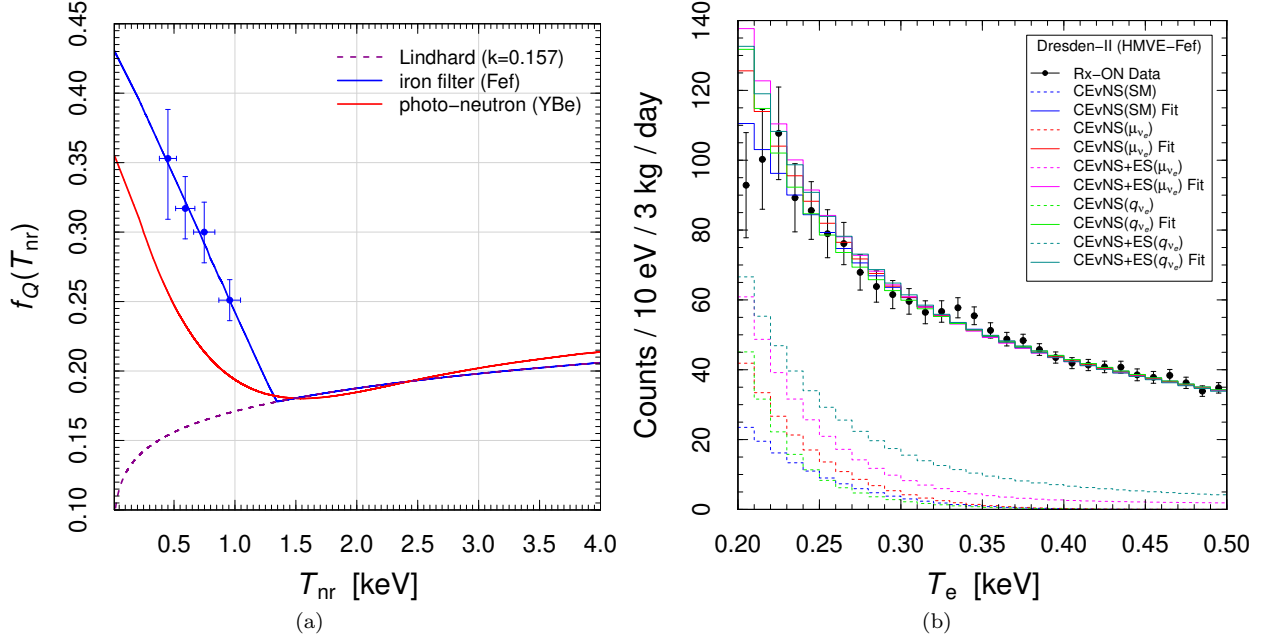


FIG. 1. (a) The germanium quenching factor models provided in Ref. [36] for the analysis of the Dresden-II data: iron filter (Fef) given by the solid blue line that fits the blue data points [77] and is extended with the Lindhard model with $k = 0.157$ [78] (dashed purple line) for $T_{nr} \gtrsim 1.35$ keV; photo-neutron (YBe) given by the solid red line. (b) Illustration of different CE ν NS and ES predictions for the Dresden-II spectrum compared with the Rx-ON data. CE ν NS (SM) is the Standard Model CE ν NS prediction. CE ν NS (μ_{ν_e}) and CE ν NS + ES(μ_{ν_e}) are, respectively, the CE ν NS (SM) plus CE ν NS and CE ν NS + ES predictions induced by $\mu_{\nu_e} = 3 \times 10^{-10} \mu_B$. CE ν NS (q_{ν_e}) is the CE ν NS (SM) plus CE ν NS prediction induced by $q_{\nu_e} = 1.5 \times 10^{-9} e$. CE ν NS + ES(q_{ν_e}) is the CE ν NS (SM) plus CE ν NS + ES prediction induced by $q_{\nu_e} = 1.3 \times 10^{-11} e$. The dashed histograms represent the predictions obtained considering the HMVE reactor antineutrino flux and Fef quenching. The solid histograms show the corresponding predictions plus fitted background.

atoms, $T_{nr}^{\min} \simeq 2.96$ eV is the minimum average ionization energy in Ge, $R(T_e, T'_e(T'_{nr}))$ is the detector energy resolution function, $T'_e(T'_{nr}) = f_Q(T'_{nr})T'_{nr}$ is the ionization energy where f_Q is the germanium quenching factor. For the latter, following the data release in Ref. [36] we consider two models based on experimental measurements. The first one determined from photo-neutron source measurements, so-called YBe [77], and the second one derived from iron-filtered monochromatic neutrons, so-called Fef, that consists in a simple linear fit of the four data points for $T_{nr} \lesssim 1.35$ keV and is extended above this range with the standard Lindhard model with $k = 0.157$ [78]. The different quenching factors are shown in Fig. 1(a) together with the experimental points used for the determination of the Fef model. The differences in the constraints derived using the two quenching factors are used as an estimate of the related uncertainty. The detector energy-resolution function is described as a truncated Gaussian

$$R(T_e, T'_e(T'_{nr})) = \left(\frac{2}{1 + \text{Erf} \left(\frac{T'_e(T'_{nr})}{\sqrt{2}\sigma'_e} \right)} \right) \frac{1}{\sqrt{2\pi}\sigma'_e} e^{-\frac{(T_e - T'_e(T'_{nr}))^2}{2\sigma'^2_e}}, \quad (31)$$

with a standard deviation equal to $\sigma'_e = \sqrt{\sigma_n^2 + \eta F_f T_e}$, where the average energy of electron-hole formation is $\eta = 2.96$ eV and the Fano factor is $F_f = 0.11$ for Ge [36]. Finally, in Eq. (30) the experimental acceptance does not appear since the data points provided in the data release are already corrected for it.

Similarly to the CsI analysis, we also include the contribution of the electron-antineutrino scattering. In

each electron-recoil energy-bin i , the theoretical ES event number N_i^{ES} is given by

$$N_i^{\text{ES}} = N(\text{Ge}) \int_{T_e^i}^{T_e^{i+1}} dT_e \int_{T_e'^{\min}}^{T_e'^{\max}} dT_e' R(T_e, T_e') \int_{E_{\min}(T_e')}^{E_{\max}} dE \frac{dN_{\bar{\nu}}}{dE}(E) \frac{d\sigma_{\bar{\nu}-\text{Ge}}^{\text{ES}}(E, T_e')}{dT_e'}, \quad (32)$$

with the difference that in the energy resolution the quenching factor must be set to unity.

We performed the analysis of the Dresden-II Ge data using the least-squares function

$$\chi_{\text{Ge}, \text{CE}\nu\text{NS}+\text{ES}}^2 = \sum_{i=1}^{130} \left(\frac{N_i^{\text{bkg}} + \alpha(N_i^{\text{CE}\nu\text{NS}} + N_i^{\text{ES}}) - N_i^{\text{exp}}}{\sigma_{\text{exp}}} \right)^2 + \left(\frac{\beta - \beta_{\text{M/L1}}}{\sigma_{\beta_{\text{M/L1}}}} \right)^2 + \left(\frac{\alpha - 1}{\sigma_{\alpha}} \right)^2, \quad (33)$$

where N_i^{bkg} , $N_i^{\text{CE}\nu\text{NS}}$ and N_i^{ES} are the predictions in the i -th electron recoil energy bin for the background, the CE ν NS signal and the ES signal, respectively, and N_i^{exp} is the experimental number of events in the i -th bin. The nuisance parameter α takes into account the uncertainty on the neutrino flux (with $\sigma_{\alpha} = 2\%$), while $\beta_{\text{M/L1}}$ is a prior for the M- to L1-shells ratio, with $\beta_{\text{M/L1}} = 0.16$ and $\sigma_{\beta_{\text{M/L1}}} = 0.03$. In this work, to appreciate the impact of the ES contribution, we will sometimes fit the Ge data set for CE ν NS only. In this case, the least-squares function $\chi_{\text{Ge}, \text{CE}\nu\text{NS}}^2$ is obtained by removing the ES contribution from Eq. (33).

In Fig. 1(b) we show the CE ν NS and ES predictions for the Dresden-II spectrum compared with the Rx-ON data under different hypotheses and with or without the inclusion of the background. In this way, one can compare the SM CE ν NS prediction, CE ν NS(SM), with the predictions obtained in presence of a possible neutrino MM, considering $\mu_{\nu_e} = 3 \times 10^{-10} \mu_{\text{B}}$, and a possible neutrino EC, considering $q_{\nu_e} = 1.5 \times 10^{-9} e$. Moreover, in Fig. 1(b) we also illustrate the impact of including the neutrino-electron elastic scattering, for the same neutrino MM value as before and for a much smaller neutrino EC, namely $q_{\nu_e} = 1.3 \times 10^{-11} e$, given that, as we already pointed out in Sec. IID, the ES process is very sensitive to a possible neutrino millicharge.

IV. RESULTS

In this section, we present the results of the fit using the COHERENT CsI and Ar data set and their combination, as well as the analysis of the Dresden-II data and its combination with COHERENT for the neutrino charge radii, electric charge and magnetic moment. We also present the DRESDEN-II results on the weak mixing angle.

A. Weak mixing angle

The weak mixing angle, ϑ_{W} , is a fundamental parameter in the theory of EW interactions. So far, many experiments measured it at different energies [43], since its value can be significantly modified in some BSM theories [79]. In particular, low-energy determinations of ϑ_{W} offer a unique role, complementary to those at high-energy, being highly sensitive to extra Z (Z') bosons predicted in grand unified theories, technicolor models, supersymmetry and string theories [80]. This underscores the need for improved experimental determinations of ϑ_{W} in the low-energy regime, where most of the measurements still suffer from large uncertainties.

As shown in Ref. [14], the uncertainty obtained for the weak mixing angle from the old CsI 2017 COHERENT data set combined with the Ar one is still very large when compared to the other determinations at low-momentum transfer. Moreover, as shown in Ref. [17], the COHERENT weak mixing angle determination is strongly correlated with the value chosen for the poorly known $R_n(\text{Cs})$ and $R_n(\text{I})$, making it necessary to fit for these parameters simultaneously in order to obtain a model-independent measurement of $\sin^2 \vartheta_{\text{W}}$. By performing a combined analysis with the so-called atomic parity violation (APV) experimental result using Cs atoms, as demonstrated in Ref. [27], it has been possible to put rather stringent constraints on the weak mixing angle while keeping into account the correlation with $R_n(\text{Cs})$.

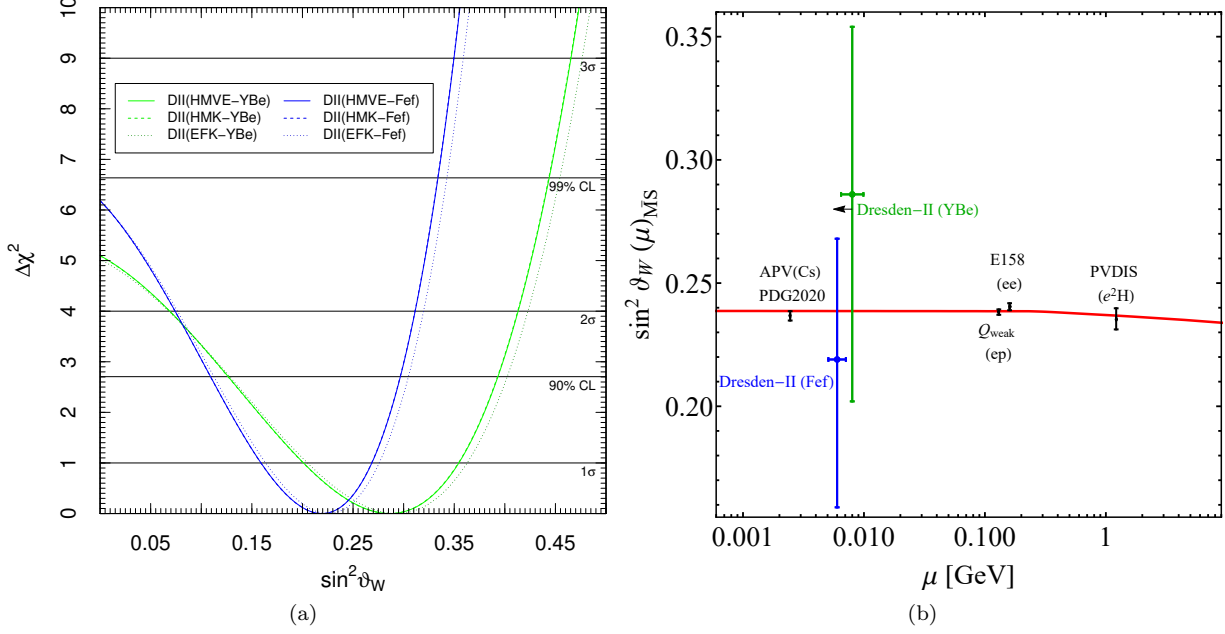


FIG. 2. (a) Marginal $\Delta\chi^2$'s for $\sin^2\vartheta_W$ obtained from the analysis of the Dresden-II data assuming the HMVE, HMK, or EFK reactor antineutrino flux and the Fef (blue) or YBe (green) quenching. (b) Variation of $\sin^2\vartheta_W$ with the energy scale μ . The SM prediction is shown as the red solid curve, together with experimental determinations in black from APV on cesium [85, 86], which has a typical momentum transfer given by $\langle Q \rangle \simeq 2.4$ MeV, Møller scattering [87] (E158), deep inelastic scattering of polarized electrons on deuterons [88] (e^2H PVDIS), and the result from the proton's weak charge at $\langle Q^2 \rangle = 0.0248$ GeV² [89] (Q_{weak}). The results derived in this paper using the Dresden-II data are shown in blue and green for the Fef and YBe quenching factor, respectively. For clarity we displayed the YBe point horizontally to the right, as indicated by the arrow.

This strong correlation between $\sin^2\vartheta_W$ and the neutron distribution rms radius applies to all EW determinations of the weak mixing angle exploiting nuclei that have been done so far, see e.g. Ref. [81]. On the contrary, as pointed out in Sec. II, in the analysis of the Dresden-II data the form factor of both protons and neutrons is practically equal to unity, making the particular choice of the value of $R_n(\text{GeV})$ completely irrelevant. Here, we show the result of a fit of the Dresden-II data aimed at the determination of the value of the weak mixing angle using three different antineutrino flux parameterizations, indicated as HMVE, HMK and EFK, and two different germanium QF functional forms, indicated as Fef and YBe. The results of these fits are summarized in Tab. III for all the six combinations of neutrino fluxes and QFs, and are depicted in Fig. 2(a). The impact of the different antineutrino fluxes is minimal. On the contrary, the impact of the different QFs is non-negligible, being the YBe results shifted to larger values of the weak mixing angle and also less precise. Focusing thus only on the HMVE flux, our results are

$$\sin^2\vartheta_W(\text{Dresden} - \text{II Fef}) = 0.219^{+0.06}_{-0.05} (1\sigma), ^{+0.11}_{-0.08} (90\%), ^{+0.14}_{-0.09} (2\sigma), \quad (34)$$

$$\sin^2\vartheta_W(\text{Dresden} - \text{II YBe}) = 0.286^{+0.08}_{-0.07} (1\sigma), ^{+0.16}_{-0.11} (90\%), ^{+0.22}_{-0.13} (2\sigma), \quad (35)$$

for the Fef and YBe quenching factors, respectively. These results are also depicted in Fig. 2(b), where a summary of the weak mixing angle measurements as a function of the energy scale μ is shown along with the SM predicted running of $\sin^2\vartheta_W$, calculated in the $\overline{\text{MS}}$ scheme [82–84].

We repeated all of the above measurements including also the ES contribution in the Dresden-II data set. However, no effect is found due to ES on the weak mixing angle, thus the results are independent of its inclusion.

Dresden-II	$\sin^2 \theta_W^{\text{b.f.}}$	1σ	90%	2σ	3σ
HMVE-Fef	0.219	(0.159, 0.268)	(0.110, 0.296)	(0.0742, 0.311)	< 0.349
HMK-Fef	0.219	(0.159, 0.268)	(0.110, 0.296)	(0.0742, 0.311)	< 0.349
EFK-Fef	0.226	(0.164, 0.275)	(0.113, 0.304)	(0.0772, 0.319)	< 0.358
HMVE-YBe	0.286	(0.202, 0.354)	(0.127, 0.393)	(0.0693, 0.413)	< 0.465
HMK-YBe	0.286	(0.201, 0.353)	(0.127, 0.392)	(0.0693, 0.412)	< 0.464
EFK-YBe	0.293	(0.206, 0.362)	(0.129, 0.402)	(0.0683, 0.423)	< 0.476

TABLE III. Best-fit value and bounds on $\sin^2 \theta_W$ obtained from the analysis of the Dresden-II data assuming the HMVE, HMK, or EFK reactor antineutrino flux and the Fef or YBe quenching.

	1σ	90%	2σ	3σ
CsI				
$\langle r_{\nu ee}^2 \rangle$	(-62, 10)	(-68, 14)	(-70, 16)	(-77, 22)
$\langle r_{\nu \mu \mu}^2 \rangle$	(-37.9, 0.5)	(-57.4, 2.9)	(-59.2, 4.4)	(-64.0, 8.6)
$ \langle r_{\nu e \mu}^2 \rangle $	< 26	< 30	< 31	< 34
$ \langle r_{\nu e \tau}^2 \rangle $	< 36	< 41	< 43	< 49
$ \langle r_{\nu \mu \tau}^2 \rangle $	< 27	< 30	< 32	< 36
Ar				
$\langle r_{\nu ee}^2 \rangle$	(-79, 29)	(-88, 38)	(-93, 43)	(-110, 59)
$\langle r_{\nu \mu \mu}^2 \rangle$	(-59.2, 8.6)	(-64.9, 14.6)	(-67.6, 17.3)	(-74.8, 24.5)
$ \langle r_{\nu e \mu}^2 \rangle $	< 33	< 36	< 38	< 44
$ \langle r_{\nu e \tau}^2 \rangle $	< 54	< 63	< 68	< 84
$ \langle r_{\nu \mu \tau}^2 \rangle $	< 34	< 40	< 42	< 50
CsI + Ar				
$\langle r_{\nu ee}^2 \rangle$	(-66, 11)	(-69, 14)	(-71, 16)	(-77, 22)
$\langle r_{\nu \mu \mu}^2 \rangle$	(-54.7, 0.8)	(-57.7, 3.2)	(-59.2, 4.7)	(-63.1, 8.3)
$ \langle r_{\nu e \mu}^2 \rangle $	< 28	< 30	< 31	< 34
$ \langle r_{\nu e \tau}^2 \rangle $	< 38	< 42	< 44	< 50
$ \langle r_{\nu \mu \tau}^2 \rangle $	< 28	< 31	< 32	< 36

TABLE IV. Bounds on the neutrino charge radii in units of 10^{-32} cm^2 obtained from the analysis of the COHERENT CsI and Ar data.

Other bounds on $\sin^2 \vartheta_W$ have also been obtained exploiting the CE ν NS data from COHERENT and Dresden-II in Ref. [90]. Although the results with the Fef QF appear to be more stringent than those presented in this work, the results are not comparable with ours because we fit the complete Dresden-II data set, whereas the analysis of Ref. [90] is a fit of the CE ν NS residual events obtained by fixing the background contribution as determined by the Dresden-II Collaboration. Such an analysis neglects the systematic uncertainties related to the background leading thus to more stringent constraints.

B. Neutrino charge radii

Bounds on the neutrino CR determined by combining the first COHERENT CsI [1] data set and the Ar [3] data set have been discussed in Ref. [14, 21]. In particular, in Ref. [21] we derived bounds on the neutrino CR using the 2017 CsI COHERENT data set and their determination of the QF, while in Ref. [14] we used the same data set but in combination with the more precise determination of the QF in Ref. [98]. In Ref. [14] we also derived constraints for the neutrino CR using the Ar data set exploiting only the CE ν NS nuclear recoil energy spectrum.

Here, we first update these limits by considering the latest CsI data release from COHERENT [5], which presented more than doubled statistics and the refined QF determination, and their combination with the

	1σ	90%	2σ	3σ
Dresden-II (HMVE-Fef)				
$\langle r_{\nu ee}^2 \rangle$	(-54, 2)	(-56, 4)	(-58, 5)	(-61, 8)
$ \langle r_{\nu e\mu}^2 \rangle , \langle r_{\nu e\tau}^2 \rangle $	< 28	< 30	< 32	< 35
Dresden-II (HMK-Fef)				
$\langle r_{\nu ee}^2 \rangle$	(-54, 2)	(-57, 4)	(-58, 5)	(-61, 8)
$ \langle r_{\nu e\mu}^2 \rangle , \langle r_{\nu e\tau}^2 \rangle $	< 28	< 30	< 31	< 35
Dresden-II (EFK-Fef)				
$\langle r_{\nu ee}^2 \rangle$	(-55, 2)	(-57, 5)	(-58, 6)	(-62, 9)
$ \langle r_{\nu e\mu}^2 \rangle , \langle r_{\nu e\tau}^2 \rangle $	< 28	< 31	< 32	< 36
Dresden-II (HMVE-YBe)				
$\langle r_{\nu ee}^2 \rangle$	(-61, 9)	(-65, 12)	(-66, 14)	(-71, 18)
$ \langle r_{\nu e\mu}^2 \rangle , \langle r_{\nu e\tau}^2 \rangle $	< 35	< 38	< 40	< 44
Dresden-II (HMK-YBe)				
$\langle r_{\nu ee}^2 \rangle$	(-61, 9)	(-65, 12)	(-66, 14)	(-71, 18)
$ \langle r_{\nu e\mu}^2 \rangle , \langle r_{\nu e\tau}^2 \rangle $	< 35	< 38	< 40	< 44
Dresden-II (EFK-YBe)				
$\langle r_{\nu ee}^2 \rangle$	(-62, 10)	(-65, 13)	(-67, 15)	(-72, 19)
$ \langle r_{\nu e\mu}^2 \rangle , \langle r_{\nu e\tau}^2 \rangle $	< 36	< 39	< 41	< 45

TABLE V. Bounds on the neutrino charge radii in units of 10^{-32} cm^2 obtained from the analysis of the Dresden-II data assuming the HMVE, HMK, or EFK reactor antineutrino flux and the Fef or YBe quenching.

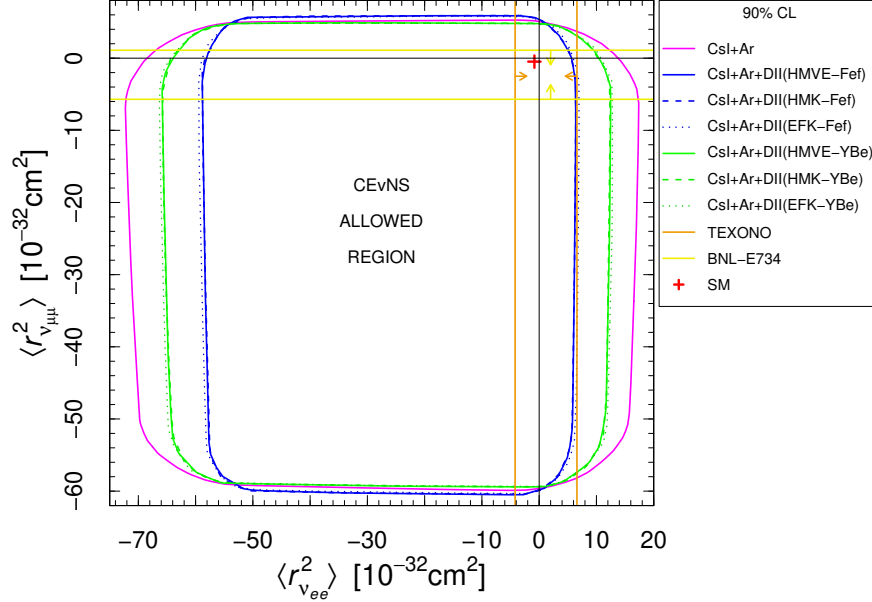


FIG. 3. Contours of the 90% C.L. allowed regions in the $(\langle r_{\nu ee}^2 \rangle, \langle r_{\nu \mu\mu}^2 \rangle)$ plane obtained from the analysis of the COHERENT CsI and Ar data (magenta), and from the combined analysis of the COHERENT data and Dresden-II data assuming the HMVE, HMK, or EFK reactor antineutrino flux and the Fef (blue) or YBe (green) quenching. The red cross near the origin indicates the Standard Model values in Eqs. (9) and (10). The orange and yellow lines delimit, respectively, the 90% bounds on $\langle r_{\nu ee}^2 \rangle$ and $\langle r_{\nu \mu\mu}^2 \rangle$ obtained in the TEXONO [91] and BNL-E734 [92] experiments.

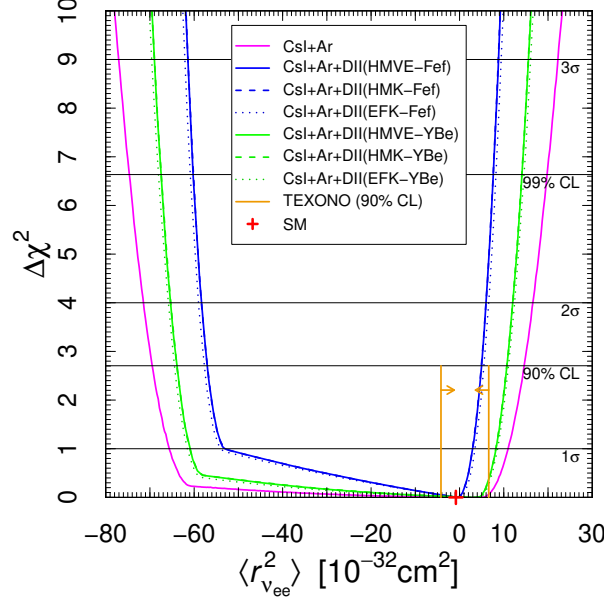


FIG. 4. Marginal $\Delta\chi^2$'s for $\langle r_{\nu ee}^2 \rangle$ obtained from the analysis of the COHERENT CsI and Ar data (magenta), and from the combined analysis of the COHERENT data and Dresden-II data assuming the HMVE, HMK, or EFK reactor antineutrino flux and the Fef (blue) or YBe (green) quenching. The red cross near the origin indicates the Standard Model value in Eq. (9). The short vertical orange lines show the lower and upper 90% bounds on $\langle r_{\nu ee}^2 \rangle$ obtained in the TEXONO [91] experiment.

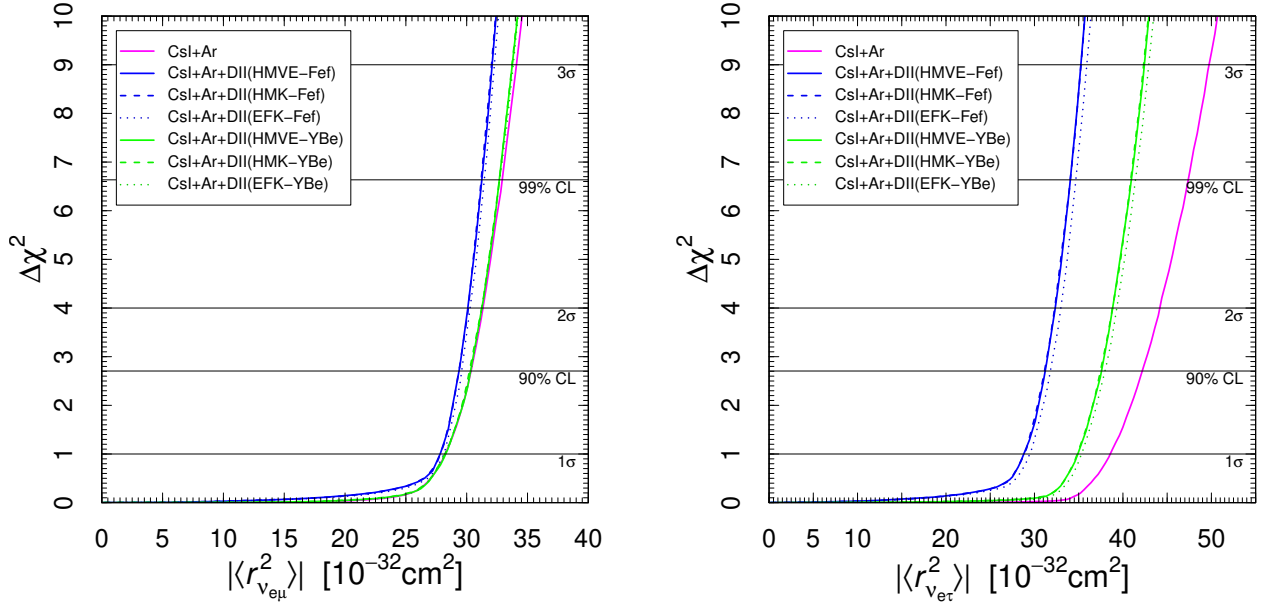


FIG. 5. Marginal $\Delta\chi^2$'s for $|\langle r_{\nu e\mu}^2 \rangle|$ and $|\langle r_{\nu e\tau}^2 \rangle|$ obtained from the analysis of the COHERENT CsI and Ar data (magenta), and from the combined analysis of the COHERENT data and Dresden-II data assuming the HMVE, HMK, or EFK reactor antineutrino flux and the Fef (blue) or YBe (green) quenching.

	1σ	90%	2σ	3σ
CsI + Ar + Dresden-II (HMVE-Fef)				
$\langle r_{\nu_{ee}}^2 \rangle$	(-52, 3)	(-56, 5)	(-58, 6)	(-61, 9)
$\langle r_{\nu_{\mu\mu}}^2 \rangle$	(-55.6, 1.8)	(-58.2, 4.0)	(-59.8, 5.1)	(-63.1, 8.7)
$ \langle r_{\nu_{e\mu}}^2 \rangle $	< 28	< 29	< 30	< 32
$ \langle r_{\nu_{e\tau}}^2 \rangle $	< 28	< 31	< 32	< 35
$ \langle r_{\nu_{\mu\tau}}^2 \rangle $	< 29	< 32	< 33	< 36
CsI + Ar + Dresden-II (HMK-Fef)				
$\langle r_{\nu_{ee}}^2 \rangle$	(-52, 3)	(-56, 5)	(-58, 6)	(-61, 9)
$\langle r_{\nu_{\mu\mu}}^2 \rangle$	(-55.8, 1.8)	(-58.4, 3.8)	(-59.8, 5.4)	(-63.3, 8.7)
$ \langle r_{\nu_{e\mu}}^2 \rangle $	< 28	< 29	< 30	< 32
$ \langle r_{\nu_{e\tau}}^2 \rangle $	< 28	< 31	< 32	< 35
$ \langle r_{\nu_{\mu\tau}}^2 \rangle $	< 29	< 31	< 33	< 36
CsI + Ar + Dresden-II (EFK-Fef)				
$\langle r_{\nu_{ee}}^2 \rangle$	(-53, 3)	(-58, 5)	(-58, 6)	(-62, 9)
$\langle r_{\nu_{\mu\mu}}^2 \rangle$	(-55.8, 1.8)	(-58.4, 4.0)	(-59.3, 4.9)	(-62.8, 8.4)
$ \langle r_{\nu_{e\mu}}^2 \rangle $	< 28	< 29	< 30	< 32
$ \langle r_{\nu_{e\tau}}^2 \rangle $	< 29	< 32	< 33	< 36
$ \langle r_{\nu_{\mu\tau}}^2 \rangle $	< 29	< 31	< 33	< 36
CsI + Ar + Dresden-II (HMVE-YBe)				
$\langle r_{\nu_{ee}}^2 \rangle$	(-60, 7)	(-63, 10)	(-65, 12)	(-69, 15)
$\langle r_{\nu_{\mu\mu}}^2 \rangle$	(-54.3, 0.74)	(-57.3, 3.2)	(-58.9, 4.3)	(-62.2, 7.8)
$ \langle r_{\nu_{e\mu}}^2 \rangle $	< 28	< 30	< 31	< 33
$ \langle r_{\nu_{e\tau}}^2 \rangle $	< 35	< 37	< 38	< 42
$ \langle r_{\nu_{\mu\tau}}^2 \rangle $	< 28	< 30	< 32	< 35
CsI + Ar + Dresden-II (HMK-YBe)				
$\langle r_{\nu_{ee}}^2 \rangle$	(-60, 8)	(-63, 10)	(-65, 12)	(-69, 15)
$\langle r_{\nu_{\mu\mu}}^2 \rangle$	(-53.8, 0.74)	(-57.1, 2.9)	(-58.4, 4.0)	(-62.2, 7.8)
$ \langle r_{\nu_{e\mu}}^2 \rangle $	< 28	< 30	< 31	< 33
$ \langle r_{\nu_{e\tau}}^2 \rangle $	< 35	< 37	< 38	< 42
$ \langle r_{\nu_{\mu\tau}}^2 \rangle $	< 28	< 30	< 32	< 35
CsI + Ar + Dresden-II (EFK-YBe)				
$\langle r_{\nu_{ee}}^2 \rangle$	(-61, 8)	(-64, 11)	(-65, 12)	(-69, 16)
$\langle r_{\nu_{\mu\mu}}^2 \rangle$	(-54.0, 0.74)	(-57.3, 2.9)	(-58.4, 4.0)	(-62.2, 7.6)
$ \langle r_{\nu_{e\mu}}^2 \rangle $	< 28	< 30	< 31	< 33
$ \langle r_{\nu_{e\tau}}^2 \rangle $	< 35	< 37	< 39	< 43
$ \langle r_{\nu_{\mu\tau}}^2 \rangle $	< 28	< 30	< 31	< 35

TABLE VI. Bounds on the neutrino charge radii in units of 10^{-32} cm² obtained from the combined analysis of the COHERENT CsI and Ar data and the Dresden-II data assuming the HMVE, HMK, or EFK reactor antineutrino flux and the Fef or YBe quenching.

Ar data set, for which we follow the data release in Ref. [4], that allowed us to also include the arrival time information. We start with the general case in which neutrinos are allowed to have both diagonal and off-diagonal CR. The results of these fits are summarized in Tab. IV. The bounds obtained for the Ar data set are of the same order of magnitude, but as expected due to statistics, less stringent than those obtained from the COHERENT CsI data. Indeed, the latter clearly dominates the combined fit, where the addition of the Ar data only makes a little improvement.

Similarly, we also fit the Dresden-II data set for the neutrino CR. In this case only $\langle r_{\nu_{ee}}^2 \rangle$, $|\langle r_{\nu_{e\mu}}^2 \rangle|$, and $|\langle r_{\nu_{e\tau}}^2 \rangle|$ could be measured by the data. As explained in Sec. IIIB, we use three different antineutrino flux parameterizations, HMVE, HMK and EFK, and two different germanium QF functional forms, Fef and YBe. The results of these fits are summarized in Tab. V for all the six combinations of neutrino fluxes and QFs. As it is possible to see, the three fluxes induce very small differences in the final bounds, while the QF plays

Process	Collaboration	Limit [10^{-32} cm^2]	C.L. Ref.
Reactor $\bar{\nu}_e$ -e	Krasnoyarsk	$ \langle r_{\nu_e}^2 \rangle < 7.3$	90% [94]
	TEXONO	$-4.2 < \langle r_{\nu_e}^2 \rangle < 6.6$	90% [91] ^a
Accelerator ν_e -e	LAMPF	$-7.12 < \langle r_{\nu_e}^2 \rangle < 10.88$	90% [95] ^a
	LSND	$-5.94 < \langle r_{\nu_e}^2 \rangle < 8.28$	90% [96] ^a
Accelerator ν_μ -e and $\bar{\nu}_\mu$ -e	BNL-E734	$-5.7 < \langle r_{\nu_\mu}^2 \rangle < 1.1$	90% [92] ^{a,b}
	CHARM-II	$ \langle r_{\nu_\mu}^2 \rangle < 1.2$	90% [97] ^a
COHERENT + Dresden-II	w/o transition CR	$-7.1 < \langle r_{\nu_e}^2 \rangle < 5$	90% This work ^c
	w transition CR	$-56 < \langle r_{\nu_e}^2 \rangle < 5$	90% This work ^c
COHERENT + Dresden-II	w/o transition CR	$-5.9 < \langle r_{\nu_\mu}^2 \rangle < 4.3$	90% This work ^c
	w transition CR	$-58.2 < \langle r_{\nu_\mu}^2 \rangle < 4.0$	90% This work ^c

^a Corrected by a factor of two due to a different convention, see Ref. [21].

^b Corrected in Ref. [93].

^c Using the Fef quenching factor.

TABLE VII. Experimental limits for the neutrino charge radii.

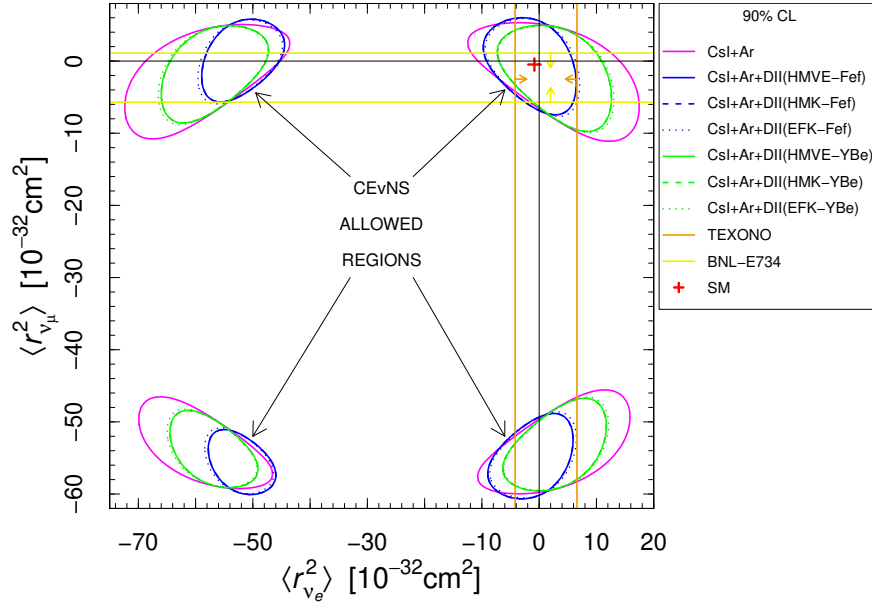


FIG. 6. Contours of the 90% C.L. allowed regions in the $(\langle r_{\nu_e}^2 \rangle, \langle r_{\nu_\mu}^2 \rangle)$ plane obtained from the analysis of the COHERENT CsI and Ar data (magenta), and from the combined analysis of the COHERENT data and Dresden-II data assuming the HMVE, HMK, or EFK reactor antineutrino flux and the Fef (blue) or YBe (green) quenching, in the absence of transition charge radii. The red cross near the origin indicates the Standard Model values in Eqs. (9) and (10). The orange and yellow lines delimit, respectively, the 90% bounds on $\langle r_{\nu_e}^2 \rangle$ and $\langle r_{\nu_\mu}^2 \rangle$ obtained in the TEXONO [91] and BNL-E734 [92] experiments.

a more important role. All in all, the bounds obtained from the Dresden-II data set are comparable with those obtained from the CsI and Ar data set, with a precision similar to the CsI data set.

Finally, in Tab. VI we show the bounds on the neutrino CR obtained from the combined analysis of the COHERENT CsI and Ar data and the Dresden-II data assuming all the six combinations of neutrino fluxes and QFs. An improvement with respect to the results obtained fitting the COHERENT data set alone is visible.

The contours of the 90% C.L. allowed regions in the $(\langle r_{\nu_{ee}}^2 \rangle, \langle r_{\nu_{\mu\mu}}^2 \rangle)$ plane obtained from the analysis of

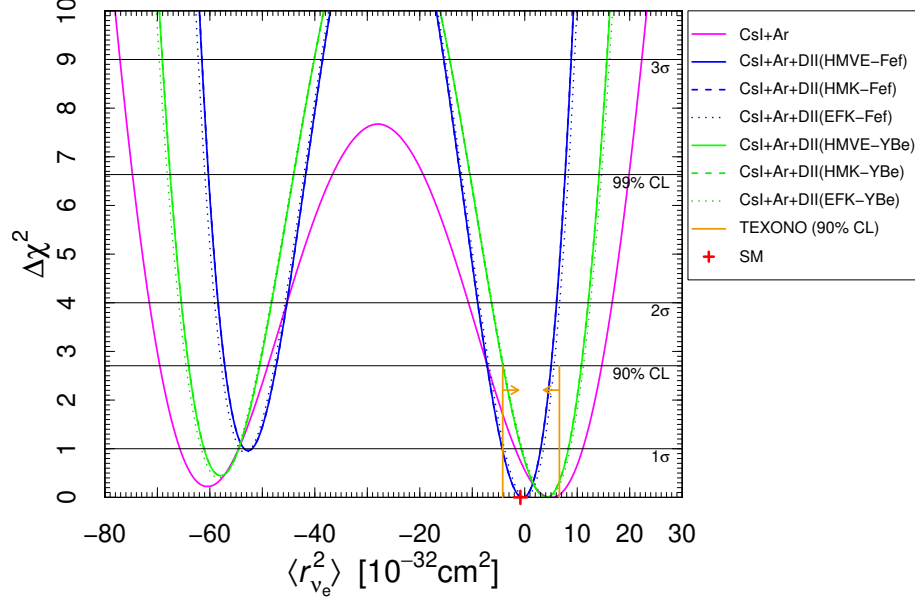


FIG. 7. Marginal $\Delta\chi^2$'s for $\langle r_{\nu_e}^2 \rangle$ obtained from the analysis of the COHERENT CsI and Ar data (magenta), and from the combined analysis of the COHERENT data and Dresden-II data assuming the HMVE, HMK, or EFK reactor antineutrino flux and the Fef (blue) or YBe (green) quenching, in the absence of transition charge radii. The red cross near the origin indicates the Standard Model value in Eq. (9). The short vertical orange lines show the lower and upper 90% bounds on $\langle r_{\nu_e}^2 \rangle$ obtained in the TEXONO [91] experiment.

	1σ	90%	2σ	3σ
CsI				
$\langle r_{\nu_e}^2 \rangle$	(-62.4, -57.2)	(-68.1, -49.4)	(-70.4, -45.1)	(-76.8, 21.6)
	(-2.9, 10.1)	(-8.6, 13.8)	(-12.4, 15.8)	
$\langle r_{\nu_\mu}^2 \rangle$	(-7.0, 0.5)	(-57.4, -49.0)	(-59.2, -46.9)	(-64.0, -41.8)
		(-9.7, 2.9)	(-11.2, 4.4)	(-16.0, 8.6)
Ar				
$\langle r_{\nu_e}^2 \rangle$	(-79.3, -37.7)	(-88.5, 38.0)	(-93.4, 43.1)	(-109.8, 59.2)
	(-12.4, 28.8)			
$\langle r_{\nu_\mu}^2 \rangle$	(-59.2, -36.4)	(-64.9, 14.6)	(-67.6, 17.3)	(-75.1, 24.5)
	(-13.9, 8.6)			
CsI + Ar				
$\langle r_{\nu_e}^2 \rangle$	(-65.5, -54.6)	(-69.3, -49.2)	(-71.3, -45.4)	(-77.0, 22.1)
	(-1.7, 10.9)	(-6.9, 14.4)	(-10.6, 16.4)	
$\langle r_{\nu_\mu}^2 \rangle$	(-54.7, -51.4)	(-57.7, -47.8)	(-59.2, -46.3)	(-63.1, -41.8)
	(-6.4, 0.8)	(-8.8, 3.2)	(-10.3, 4.7)	(-14.8, 8.6)

TABLE VIII. Bounds on the diagonal neutrino charge radii in units of 10^{-32} cm^2 obtained from the analysis of the COHERENT CsI and Ar data in the absence of transition charge radii.

the COHERENT CsI and Ar data, and from the combined analysis of the COHERENT data and Dresden-II data assuming the HMVE, HMK, or EFK reactor antineutrino flux and the Fef or YBe quenching are shown in Fig. 3 together with the SM values in Eqs. (9) and (10) and the 90% bounds on $\langle r_{\nu_{ee}}^2 \rangle$ and $\langle r_{\nu_{\mu\mu}}^2 \rangle$ obtained, respectively, in the TEXONO [91] and BNL-E734 [92] experiments. In Fig. 4 we show the marginal $\Delta\chi^2$'s for $\langle r_{\nu_{ee}}^2 \rangle$ together with the SM value in Eq. (9) and the lower and upper 90% bounds on $\langle r_{\nu_{ee}}^2 \rangle$ obtained in the TEXONO [91] experiment. As visible, the point corresponding to the SM values of the diagonal

	1σ	90%	2σ	3σ
Dresden-II (HMVE-Fef)				
$\langle r_{\nu_e}^2 \rangle$	(-54.3, -45.0) (-7.4, 1.6)	(-56.7, -40.8) (-11.6, 4.0)	(-58.0, -38.0) (-14.7, 5.4)	(-61.1, 8.4)
Dresden-II (HMK-Fef)				
$\langle r_{\nu_e}^2 \rangle$	(-54.3, -45.0) (-7.4, 1.6)	(-56.7, -40.8) (-11.6, 4.0)	(-57.8, -38.0) (-14.7, 5.4)	(-61.1, 8.4)
Dresden-II (EFK-Fef)				
$\langle r_{\nu_e}^2 \rangle$	(-54.9, -45.5) (-7.2, 2.3)	(-57.3, -41.3) (-11.4, 4.7)	(-58.7, -38.2) (-14.4, 6.0)	(-62.0, 9.3)
Dresden-II (HMVE-YBe)				
$\langle r_{\nu_e}^2 \rangle$	(-61.5, -48.5) (-3.9, 8.9)	(-64.8, -42.4) (-10.3, 12.2)	(-66.4, -37.5) (-15.1, 13.9)	(-70.8, 18.3)
Dresden-II (HMK-YBe)				
$\langle r_{\nu_e}^2 \rangle$	(-61.5, -48.5) (-3.9, 8.9)	(-64.8, -42.4) (-10.3, 12.2)	(-66.4, -37.5) (-15.1, 13.7)	(-70.8, 18.1)
Dresden-II (EFK-YBe)				
$\langle r_{\nu_e}^2 \rangle$	(-62.2, -49.0) (-3.7, 9.5)	(-65.5, -42.6) (-10.0, 12.8)	(-67.2, -37.5) (-15.1, 14.6)	(-71.9, 19.2)

TABLE IX. Bounds on the electron neutrino charge radius $\langle r_{\nu_e}^2 \rangle$ in units of 10^{-32} cm^2 obtained from the analysis of the Dresden-II data assuming the HMVE, HMK, or EFK reactor antineutrino flux and the Fef or YBe quenching in the absence of transition charge radii.

CR lies at the edge of the 1σ allowed region and very close to the best fit value for $\langle r_{\nu_{ee}}^2 \rangle$ in the combined CsI+Ar+Dresden-II fit. For a better comparison, in Tab. VII we report a summary of the most recent and precise bounds on $\langle r_{\nu_{ee}}^2 \rangle$ and $\langle r_{\nu_{\mu\mu}}^2 \rangle$. Please note that some of these limits have been corrected by a factor of two due to a different convention, see Ref. [21] for a detailed explanation. In Tab. VII we also summarized the results found in this work from the combined Dresden-II + COHERENT analysis when considering non-null transition CR. Interestingly, we are able to improve the best upper bound limit for $\langle r_{\nu_{ee}}^2 \rangle$ previously set by TEXONO. Finally, in Fig. 5 we show the marginal $\Delta\chi^2$'s for $|\langle r_{\nu_{e\mu}}^2 \rangle|$ and $|\langle r_{\nu_{e\tau}}^2 \rangle|$, for which, especially in the latter case, the Fef QF permits to obtain significantly more stringent bounds.

We also assumed the absence of transition CR, fitting thus only for the diagonal charge radii $\langle r_{\nu_e}^2 \rangle \equiv \langle r_{\nu_{ee}}^2 \rangle$ and $\langle r_{\nu_\mu}^2 \rangle \equiv \langle r_{\nu_{\mu\mu}}^2 \rangle$. In this way we probe the values of the neutrino CR in the SM. However, since it is also possible that BSM physics generates off-diagonal neutrino CR that are much smaller than the diagonal ones and that can thus be neglected in a first approximation, also new physics models can be tested in this scenario. The bounds are shown in Tabs. VIII, IX and X from the analysis of COHERENT data only, Dresden-II data only for the different reactor antineutrino fluxes and germanium QFs (only $\langle r_{\nu_e}^2 \rangle$ can be tested in this case) and their combinations, respectively. The corresponding contours of the 90% C.L. allowed regions in the $(\langle r_{\nu_e}^2 \rangle, \langle r_{\nu_\mu}^2 \rangle)$ plane are shown in Fig. 6. One can see that the contribution of the Dresden-II data leads to a considerable restriction of the allowed regions, especially when using the Fef QF. Here, we also show the SM values in Eqs. (9) and (10) and the 90% bounds on $\langle r_{\nu_e}^2 \rangle$ and $\langle r_{\nu_\mu}^2 \rangle$ obtained, respectively, in the TEXONO [91] and BNL-E734 [92] experiments. In Fig. 7 we also show the marginal $\Delta\chi^2$'s for $\langle r_{\nu_e}^2 \rangle$. As summarized in Tab. VII, assuming the absence of the transition CR we obtain a very competitive limit at 90% C.L. with respect to that set by TEXONO when using the Fef QF, namely

$$-7.1 < \langle r_{\nu_e}^2 \rangle < 5, \quad (36)$$

in units of 10^{-32} cm^2 . In particular, we are able to restrict the upper bound limit from $6.6 \times 10^{-32} \text{ cm}^2$ to $5 \times 10^{-32} \text{ cm}^2$. When using the YBe QF, the limit becomes $-4.1 < \langle r_{\nu_e}^2 \rangle < 10.8$ in units of 10^{-32} cm^2 , with a slightly better lower bound with respect to that set by TEXONO. In both cases, the limits obtained are practically independent of the particular reactor antineutrino flux used.

We repeated all of the above bound calculations including also the ES contribution for the CsI and Dresden-II data set. However, no effect is found due to ES on the neutrino CR, thus the results are independent of

	1σ	90%	2σ	3σ
CsI + Ar + Dresden-II (HMVE-Fef)				
$\langle r_{\nu_e}^2 \rangle$	(-53.5, -52.1)	(-57.0, -47.4)	(-58.4, -45.3)	(-61.4, -38.6)
	(-4.2, 2.9)	(-7.1, 5.0)	(-8.9, 5.9)	(-15.4, 8.8)
$\langle r_{\nu_\mu}^2 \rangle$	(-56.2, -52.9)	(-58.9, -50.5)	(-60.0, -49.4)	(-63.5, -46.3)
	(-3.9, 2.3)	(-5.9, 4.3)	(-7.0, 5.4)	(-10.0, 8.9)
CsI + Ar + Dresden-II (HMK-Fef)				
$\langle r_{\nu_e}^2 \rangle$	(-53.3, -52.1)	(-57.0, -47.4)	(-58.3, -45.3)	(-61.4, -38.6)
	(-4.2, 2.9)	(-7.1, 5.0)	(-8.9, 5.9)	(-15.4, 8.7)
$\langle r_{\nu_\mu}^2 \rangle$	(-56.2, -52.9)	(-58.9, -50.5)	(-60.0, -49.4)	(-63.5, -46.3)
	(-3.9, 2.3)	(-5.9, 4.3)	(-7.0, 5.4)	(-10.0, 8.9)
CsI + Ar + Dresden-II (EFK-Fef)				
$\langle r_{\nu_e}^2 \rangle$	(-54.3, -52.2)	(-57.7, -47.8)	(-59.0, -45.8)	(-62.1, -38.9)
	(-3.8, 3.5)	(-6.7, 5.5)	(-8.5, 6.6)	(-15.1, 9.4)
$\langle r_{\nu_\mu}^2 \rangle$	(-56.2, -52.9)	(-58.7, -50.3)	(-60.0, -49.2)	(-63.3, -45.9)
	(-4.1, 2.1)	(-6.1, 4.0)	(-7.2, 5.4)	(-10.3, 8.7)
CsI + Ar + Dresden-II (HMVE-YBe)				
$\langle r_{\nu_e}^2 \rangle$	(-61.0, -54.6)	(-63.9, -50.6)	(-65.4, -48.4)	(-69.0, -40.3)
	(-0.52, 8.3)	(-4.1, 10.8)	(-6.3, 12.0)	(-14.3, 15.6)
$\langle r_{\nu_\mu}^2 \rangle$	(-54.7, -51.6)	(-57.6, -48.8)	(-58.9, -47.4)	(-62.4, -43.5)
	(-5.6, 0.96)	(-7.8, 3.2)	(-9.2, 4.3)	(-12.9, 8.0)
CsI + Ar + Dresden-II (HMK-YBe)				
$\langle r_{\nu_e}^2 \rangle$	(-61.0, -54.6)	(-63.9, -50.6)	(-65.3, -48.4)	(-69.0, -40.1)
	(-0.52, 8.3)	(-4.1, 10.8)	(-6.3, 12.0)	(-14.3, 15.6)
$\langle r_{\nu_\mu}^2 \rangle$	(-54.7, -51.6)	(-57.6, -48.8)	(-58.9, -47.4)	(-62.6, -43.5)
	(-5.6, 0.96)	(-7.8, 3.2)	(-9.2, 4.3)	(-12.9, 8.0)
CsI + Ar + Dresden-II (EFK-YBe)				
$\langle r_{\nu_e}^2 \rangle$	(-61.6, -54.7)	(-64.5, -50.8)	(-65.8, -48.5)	(-69.5, -40.3)
	(-0.39, 8.6)	(-4.0, 11.2)	(-6.2, 12.4)	(-14.1, 16.1)
$\langle r_{\nu_\mu}^2 \rangle$	(-54.7, -51.6)	(-57.6, -48.5)	(-58.9, -47.2)	(-62.4, -43.3)
	(-5.9, 0.74)	(-8.1, 2.9)	(-9.4, 4.3)	(-13.1, 7.8)

TABLE X. Bounds on the diagonal neutrino charge radii in units of 10^{-32} cm^2 obtained from the combined analysis the COHERENT CsI and Ar data and the Dresden-II data assuming the HMVE, HMK, or EFK reactor antineutrino flux and the Fef or YBe quenching in the absence of transition charge radii.

its inclusion.

	1σ	90%	2σ	3σ
CsI (CEvNS)				
$q_{\nu ee}$	$(-1.6, 45.2) \times 10^{-8}$	$(-1.6, 5.8) \times 10^{-7}$	$(-1.9, 6.2) \times 10^{-7}$	$(-2.6, 7.0) \times 10^{-7}$
$q_{\nu \mu \mu}$	$(-8.0, 136.0) \times 10^{-9}$	$(-3.2, 25.2) \times 10^{-8}$	$(-4.4, 30.8) \times 10^{-8}$	$(-8.4, 43.2) \times 10^{-8}$
$ q_{\nu e \mu} $	$< 1.8 \times 10^{-7}$	$< 2.3 \times 10^{-7}$	$< 2.5 \times 10^{-7}$	$< 2.9 \times 10^{-7}$
$ q_{\nu e \tau} $	$(1.5, 4.0) \times 10^{-7}$	$< 4.3 \times 10^{-7}$	$< 4.6 \times 10^{-7}$	$< 5.2 \times 10^{-7}$
$ q_{\nu \mu \tau} $	$< 1.8 \times 10^{-7}$	$< 2.3 \times 10^{-7}$	$< 2.5 \times 10^{-7}$	$< 3.0 \times 10^{-7}$
CsI (CEvNS+ES)				
$q_{\nu ee}$	$(-3.6, 3.6) \times 10^{-10}$	$(-5.0, 5.0) \times 10^{-10}$	$(-5.6, 5.6) \times 10^{-10}$	$(-7.5, 7.5) \times 10^{-10}$
$q_{\nu \mu \mu}$	$(-1.2, 1.2) \times 10^{-10}$	$(-1.9, 1.9) \times 10^{-10}$	$(-2.2, 2.2) \times 10^{-10}$	$(-3.2, 3.2) \times 10^{-10}$
$ q_{\nu e \mu} $	$< 1.2 \times 10^{-10}$	$< 1.8 \times 10^{-10}$	$< 2.2 \times 10^{-10}$	$< 3.1 \times 10^{-10}$
$ q_{\nu e \tau} $	$< 3.5 \times 10^{-10}$	$< 5.0 \times 10^{-10}$	$< 5.6 \times 10^{-10}$	$< 7.5 \times 10^{-10}$
$ q_{\nu \mu \tau} $	$< 1.2 \times 10^{-10}$	$< 1.9 \times 10^{-10}$	$< 2.2 \times 10^{-10}$	$< 3.2 \times 10^{-10}$
Ar (CEvNS)				
$q_{\nu ee}$	$(-1.3, 1.7) \times 10^{-7}$	$(-1.7, 3.2) \times 10^{-7}$	$(-2.0, 3.5) \times 10^{-7}$	$(-2.7, 4.4) \times 10^{-7}$
$q_{\nu \mu \mu}$	$(-4.4, 10.0) \times 10^{-8}$	$(-6.8, 21.6) \times 10^{-8}$	$(-8.0, 24.4) \times 10^{-8}$	$(-1.2, 3.0) \times 10^{-7}$
$ q_{\nu e \mu} $	$< 1.0 \times 10^{-7}$	$< 1.4 \times 10^{-7}$	$< 1.5 \times 10^{-7}$	$< 1.8 \times 10^{-7}$
$ q_{\nu e \tau} $	$< 2.0 \times 10^{-7}$	$< 2.5 \times 10^{-7}$	$< 2.8 \times 10^{-7}$	$< 3.6 \times 10^{-7}$
$ q_{\nu \mu \tau} $	$< 1.1 \times 10^{-7}$	$< 1.5 \times 10^{-7}$	$< 1.7 \times 10^{-7}$	$< 2.1 \times 10^{-7}$
CsI (CEvNS) + Ar (CEvNS)				
$q_{\nu ee}$	$(-12.4, 8.0) \times 10^{-8}$	$(-1.6, 1.7) \times 10^{-7}$	$(-1.7, 2.2) \times 10^{-7}$	$(-2.2, 3.5) \times 10^{-7}$
$q_{\nu \mu \mu}$	$(-1.2, 7.6) \times 10^{-8}$	$(-3.2, 11.2) \times 10^{-8}$	$(-4.0, 12.8) \times 10^{-8}$	$(-6.8, 18.4) \times 10^{-8}$
$ q_{\nu e \mu} $	$< 1.1 \times 10^{-7}$	$< 1.4 \times 10^{-7}$	$< 1.5 \times 10^{-7}$	$< 1.9 \times 10^{-7}$
$ q_{\nu e \tau} $	$< 2.4 \times 10^{-7}$	$< 2.9 \times 10^{-7}$	$< 3.1 \times 10^{-7}$	$< 3.7 \times 10^{-7}$
$ q_{\nu \mu \tau} $	$< 1.2 \times 10^{-7}$	$< 1.5 \times 10^{-7}$	$< 1.6 \times 10^{-7}$	$< 2.0 \times 10^{-7}$
CsI (CEvNS+ES) + Ar (CEvNS)				
$q_{\nu ee}$	$(-3.5, 3.5) \times 10^{-10}$	$(-5.0, 5.0) \times 10^{-10}$	$(-5.6, 5.6) \times 10^{-10}$	$(-7.5, 7.5) \times 10^{-10}$
$q_{\nu \mu \mu}$	$(-1.2, 1.2) \times 10^{-10}$	$(-1.9, 1.9) \times 10^{-10}$	$(-2.2, 2.2) \times 10^{-10}$	$(-3.2, 3.2) \times 10^{-10}$
$ q_{\nu e \mu} $	$< 1.2 \times 10^{-10}$	$< 1.8 \times 10^{-10}$	$< 2.2 \times 10^{-10}$	$< 3.1 \times 10^{-10}$
$ q_{\nu e \tau} $	$< 3.6 \times 10^{-10}$	$< 5.0 \times 10^{-10}$	$< 5.6 \times 10^{-10}$	$< 7.5 \times 10^{-10}$
$ q_{\nu \mu \tau} $	$< 1.2 \times 10^{-10}$	$< 1.9 \times 10^{-10}$	$< 2.2 \times 10^{-10}$	$< 3.2 \times 10^{-10}$

TABLE XI. Bounds on the neutrino electric charges in units of the elementary charge e obtained from the analysis of the COHERENT CsI and Ar data. We show the results of the analyses of CsI data with CEvNS only interactions and with CEvNS+ES interactions.

C. Neutrino electric charge

There are five electric charges that can be determined with the COHERENT CEvNS data: the two diagonal EC $q_{\nu ee}$ and $q_{\nu \mu \mu}$, and the absolute values of the three transition EC $q_{\nu e \mu} = q_{\nu \mu e}^*$, $q_{\nu e \tau}$, and $q_{\nu \mu \tau}$. Using the Dresden-II data instead, only $q_{\nu ee}$, $|q_{\nu e \mu}|$, $|q_{\nu e \tau}|$ can be tested.

In this section, we present the constraints on the neutrino EC. The results of our analyses are shown in Tab. XI and Tab. XII for the COHERENT CsI and Ar data set and for the Dresden-II data, respectively. Focusing on the results shown in Tab. XI, differently from the analysis of the neutrino CR, the contribution of Ar data is dominant in the combined COHERENT analysis of the neutrino electric charges, although the CsI data set has more statistics. It follows from the enhancement of the neutrino electric charge effect in CEvNS at low q^2 , because of the denominator in Eq. (18). However, the expected enhancement due to the different CsI and Ar masses, is mitigated by the different sizes of the energy bins: in the Ar experiment the first bin includes energies from the threshold, of about 5 keV_{nr}, to about 36 keV_{nr}, whereas the first CsI energy bin have a much smaller size. Therefore, the enhancement of the EC effect occurs only in the first energy bin of the Ar experiment. Nevertheless, this enhancement is sufficient to achieve a slightly better performance of the Ar data in constraining the neutrino EC in spite of the larger uncertainties. In Tab. XI we also explicitly show the impact of including the ES in the CsI analysis, also when combining it with Ar. Thanks to the presence of the q^2 term in the denominator of Eq. (18), a large improvement of more than 2

	1σ	90%	2σ	3σ
Dresden-II (HMVE-Fef CEvNS)				
$q_{\nu ee}$	$(-1.5, 10.1) \times 10^{-10}$	$(-3.4, 12.5) \times 10^{-10}$	$(-4.3, 13.6) \times 10^{-10}$	$(-6.5, 16.0) \times 10^{-10}$
$ q_{\nu e\mu} , q_{\nu e\tau} $	$< 6.0 \times 10^{-10}$	$< 8.2 \times 10^{-10}$	$< 9.1 \times 10^{-10}$	$< 1.1 \times 10^{-9}$
Dresden-II (HMVE-Fef CEvNS+ES)				
$q_{\nu ee}$	$(-7.3, 7.6) \times 10^{-12}$	$(-9.3, 9.5) \times 10^{-12}$	$(-1.0, 1.0) \times 10^{-11}$	$(-1.2, 1.3) \times 10^{-11}$
$ q_{\nu e\mu} , q_{\nu e\tau} $	$< 7.4 \times 10^{-12}$	$< 9.4 \times 10^{-12}$	$< 1.0 \times 10^{-11}$	$< 1.3 \times 10^{-11}$
Dresden-II (HMK-Fef CEvNS+ES)				
$q_{\nu ee}$	$(-6.6, 7.0) \times 10^{-12}$	$(-8.6, 8.7) \times 10^{-12}$	$(-9.4, 9.5) \times 10^{-12}$	$(-1.1, 1.2) \times 10^{-11}$
$ q_{\nu e\mu} , q_{\nu e\tau} $	$< 6.8 \times 10^{-12}$	$< 8.6 \times 10^{-12}$	$< 9.4 \times 10^{-12}$	$< 1.2 \times 10^{-11}$
Dresden-II (EFK-Fef CEvNS+ES)				
$q_{\nu ee}$	$(-7.4, 7.7) \times 10^{-12}$	$(-9.2, 9.4) \times 10^{-12}$	$(-1.0, 1.0) \times 10^{-11}$	$(-1.2, 1.2) \times 10^{-11}$
$ q_{\nu e\mu} , q_{\nu e\tau} $	$< 7.5 \times 10^{-12}$	$< 9.4 \times 10^{-12}$	$< 1.0 \times 10^{-11}$	$< 1.2 \times 10^{-11}$
Dresden-II (HMVE-YBe CEvNS)				
$q_{\nu ee}$	$(-4.8, 12.4) \times 10^{-10}$	$(-6.6, 15.2) \times 10^{-10}$	$(-7.5, 16.3) \times 10^{-10}$	$(-9.8, 18.9) \times 10^{-10}$
$ q_{\nu e\mu} , q_{\nu e\tau} $	$< 8.9 \times 10^{-10}$	$< 1.1 \times 10^{-9}$	$< 1.2 \times 10^{-9}$	$< 1.4 \times 10^{-9}$
Dresden-II (HMVE-YBe CEvNS+ES)				
$q_{\nu ee}$	$(-1.1, 1.1) \times 10^{-11}$	$(-1.2, 1.3) \times 10^{-11}$	$(-1.3, 1.3) \times 10^{-11}$	$(-1.5, 1.5) \times 10^{-11}$
$ q_{\nu e\mu} , q_{\nu e\tau} $	$< 1.1 \times 10^{-11}$	$< 1.2 \times 10^{-11}$	$< 1.3 \times 10^{-11}$	$< 1.5 \times 10^{-11}$
Dresden-II (HMK-YBe CEvNS+ES)				
$q_{\nu ee}$	$(-9.9, 10.2) \times 10^{-12}$	$(-1.1, 1.2) \times 10^{-11}$	$(-1.2, 1.2) \times 10^{-11}$	$(-1.4, 1.4) \times 10^{-11}$
$ q_{\nu e\mu} , q_{\nu e\tau} $	$< 1.0 \times 10^{-11}$	$< 1.1 \times 10^{-11}$	$< 1.2 \times 10^{-11}$	$< 1.4 \times 10^{-11}$
Dresden-II (EFK-YBe CEvNS+ES)				
$q_{\nu ee}$	$(-1.0, 1.1) \times 10^{-11}$	$(-1.2, 1.2) \times 10^{-11}$	$(-1.3, 1.3) \times 10^{-11}$	$(-1.4, 1.4) \times 10^{-11}$
$ q_{\nu e\mu} , q_{\nu e\tau} $	$< 1.1 \times 10^{-11}$	$< 1.2 \times 10^{-11}$	$< 1.3 \times 10^{-11}$	$< 1.4 \times 10^{-11}$

TABLE XII. Bounds on the neutrino electric charges in units of the elementary charge e obtained from the analysis of the Dresden-II data assuming the HMVE, HMK, or EFK reactor antineutrino flux and the Fef or YBe quenching. For the HMVE reactor antineutrino flux we show the results obtained with CEvNS only interactions and with CEvNS+ES interactions.

orders of magnitude with respect to the limits derived ignoring the ES contribution is obtained.

In Tab. XII we show the bounds on the EC found using the Dresden-II data. As for the neutrino CR limits discussed above, the different flux parameterizations cause only negligible differences in the obtained bounds. Thus, for the case in which we fit exclusively for the CEvNS contribution, we show only the results obtained with the HMVE flux, while when we include the ES contribution we show all the three different parameterizations. As already stated in Sec. IID, the $|q^2|$ corresponding to ES is much smaller than the CEvNS $|q^2|$, resulting in improved sensitivity when the ES contribution is included with respect to CEvNS only. Namely, with CEvNS only there is an improvement with respect to COHERENT CEvNS only of about 2 orders of magnitude, while with CEvNS + ES the improvement is of about 4 orders of magnitude.

In Fig. 8 we show the marginal $\Delta\chi^2$'s for $|q_{\nu ee}|$ obtained from the separate analyses of the COHERENT Ar and CsI data and their combinations, with CEvNS interactions only and with the ES contribution, as well as the CEvNS-only analyses of Dresden-II data assuming the HMVE reactor antineutrino flux and the YBe or Fef QF. Moreover, also the CEvNS + ES analysis of Dresden-II data assuming the HMVE, HMK, or EFK reactor antineutrino flux and the YBe or Fef QF is drawn. We also show the 90% C.L. upper bounds on $|q_{\nu ee}|$ obtained, respectively, in Ref. [99] from TEXONO data [100], in Ref. [101] from the GEMMA [102] bound on $|\mu_{\nu e}|$, and in Ref. [103] from TEXONO data [104] and GEMMA data [102]. Intriguingly, the bounds on $|q_{\nu ee}|$ obtained from the combination of COHERENT with the Dresden-II CEvNS + ES data set are much more stringent than the COHERENT ones and the CEvNS only fit, namely at 90% C.L. and using the Fef quenching factor

$$-9.3 < q_{\nu ee} < 9.5, \quad (37)$$

in units of $10^{-12} e$. This limit is competitive with respect to the other aforementioned bounds, that are at the level of $10^{-12} e$, the best limit being $|q_{\nu ee}| < 1.0 \times 10^{-12} e$ [103]. However, when comparing these limits

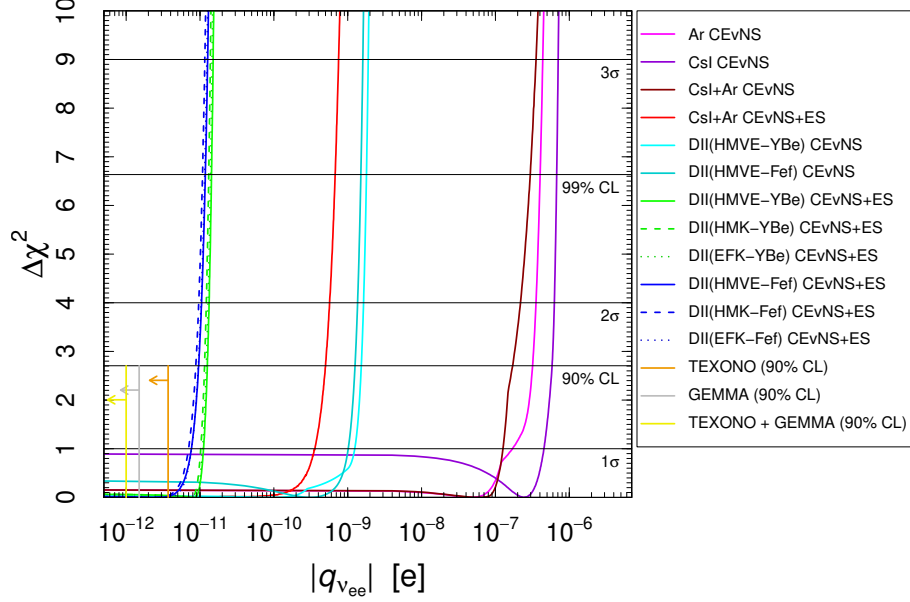


FIG. 8. Marginal $\Delta\chi^2$'s for $|q_{\nu ee}|$ obtained from: the separate analyses of the COHERENT Ar (magenta) and CsI (darkviolet) data with $\text{CE}\nu\text{NS}$ interactions; the combined analyses of the COHERENT Ar and CsI data with $\text{CE}\nu\text{NS}$ interactions only (dark red) and with $\text{CE}\nu\text{NS} + \text{ES}$ interactions (red); the $\text{CE}\nu\text{NS}$ -only analyses of Dresden-II data assuming the HMVE reactor antineutrino flux and the YBe (cyan) or Fef (dark cyan) quenching; the $\text{CE}\nu\text{NS} + \text{ES}$ analyses of Dresden-II data assuming the HMVE, HMK, or EFK reactor antineutrino flux and the YBe (green) or Fef (blue) quenching. The short vertical orange, gray, and yellow lines show the 90% C.L. upper bounds on $|q_{\nu ee}|$ obtained, respectively, in Ref. [99] from TEXONO data [100], in Ref. [101] from the GEMMA [102] bound on $|\mu_{\nu e}|$, and in Ref. [103] from TEXONO data [104] and GEMMA data [102].

one has to keep in mind that, differently from this work, the limits in Ref. [103] have been derived using for the neutrino-electron cross section the MCRRPA theory [61–63]. As discussed in Sec. II A, this becomes relevant for data from Ge detectors at sub-keV sensitivities and allows them to achieve more stringent limits with respect to FEA in particular for the neutrino EC. Thus, the limits obtained in this work can be considered as very conservative and we will investigate the impact of using a random-phase approximation theory in a future work.

In Fig. 9(a) and (b) we show the marginal $\Delta\chi^2$'s for $|q_{\nu e\mu}|$ and $|q_{\nu e\tau}|$, respectively, obtained from the separate analyses of the COHERENT Ar and CsI data with $\text{CE}\nu\text{NS}$ interactions and the combined analyses of the COHERENT Ar and CsI data with $\text{CE}\nu\text{NS}$ interactions only and with the ES contribution, as well as the $\text{CE}\nu\text{NS}$ -only analyses of the Dresden-II data assuming the HMVE reactor antineutrino flux and the two QFs, and the $\text{CE}\nu\text{NS} + \text{ES}$ analyses of Dresden-II data assuming the HMVE, HMK, or EFK reactor antineutrino flux and the two QFs. Also in this case it is possible to see that the different fluxes result in negligible differences, while the impact of the QF is visible. Again, the inclusion of the ES contribution significantly improves the bounds obtained for both Dresden-II and COHERENT.

Finally, in Fig. 10(a) and (b) we show similar marginal $\Delta\chi^2$'s $|q_{\nu\mu\mu}|$ and $|q_{\nu\mu\tau}|$, respectively, using COHERENT data only. Here, together with the various bounds obtained in this work we also show the 90% C.L. upper bounds on $|q_{\nu\mu\mu}|$ obtained, respectively, in Ref. [105] from the LSND [96] bound on $|\mu_{\nu\mu}|$ and in the XMASS-I experiment [106] from solar neutrino ES.¹ Also in this case, the inclusion of the ES contribution

¹ Also in the case of the XMASS-I limit, that is the most stringent one for $|q_{\nu\mu\mu}|$, the electron-neutrino cross section is derived using an ab-initio multi-configuration relativistic random phase approximation [106] that allows them to set more stringent limits.

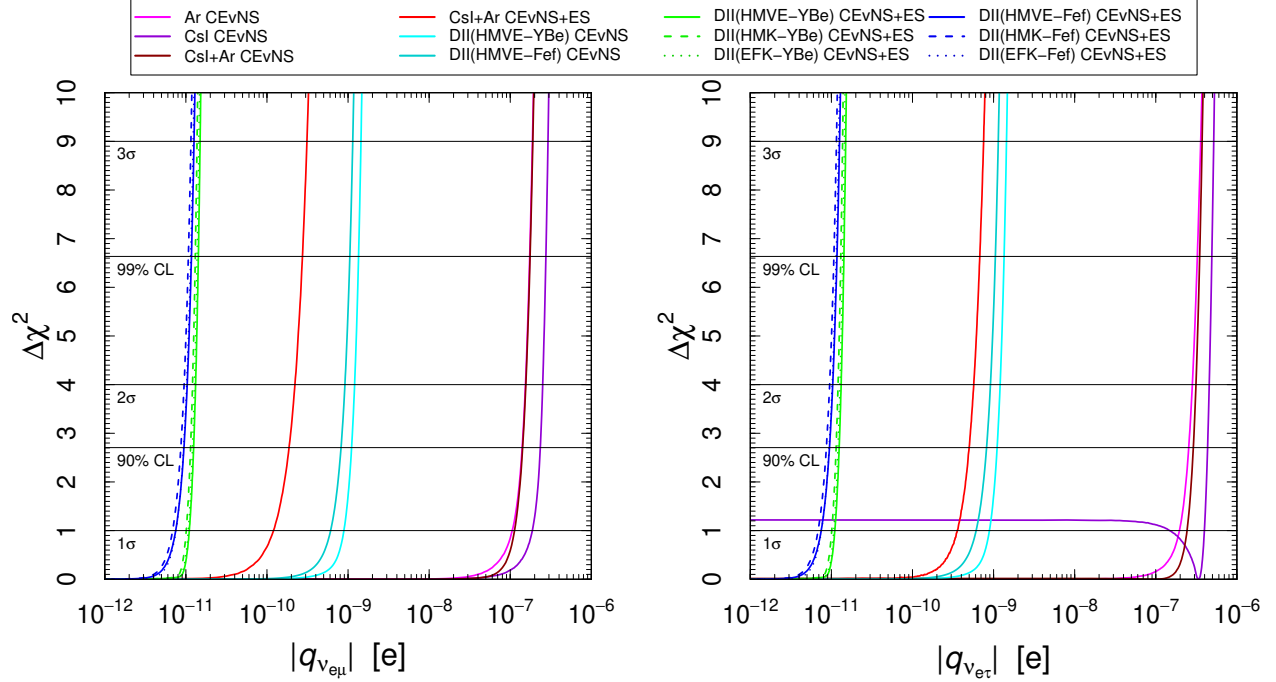


FIG. 9. Marginal $\Delta\chi^2$'s for $|q_{\nu e\mu}|$ and $|q_{\nu e\tau}|$ obtained from: the separate analyses of the COHERENT Ar (magenta) and CsI (darkviolet) data with CE ν NS interactions; the combined analyses of the COHERENT Ar and CsI data with CE ν NS interactions only (dark red) and with CE ν NS + ES interactions (red); the CE ν NS-only analyses of Dresden-II data assuming the HMVE reactor antineutrino flux and the YBe (cyan) or Fef (dark cyan) quenching; the CE ν NS + ES analyses of Dresden-II data assuming the HMVE, HMK, or EFK reactor antineutrino flux and the YBe (green) or Fef (blue) quenching.

significantly improves the bounds obtained for COHERENT, superseding the existing bounds from LSND concerning $|q_{\nu e\mu}|$, while our bounds represent the only existing laboratory bounds for $|q_{\nu e\tau}|$.

D. Neutrino magnetic moment

Finally, we study the bounds on the neutrino MM, namely on $|\mu_{\nu_e}|$ and $|\mu_{\nu_\mu}|$ using the COHERENT data and $|\mu_{\nu_e}|$ only using the Dresden-II data. The results of our analysis for the neutrino MM are shown in Tab. XIII and Tab. XIV for COHERENT CsI and Ar data set and for the Dresden-II data, respectively. In both cases, we separate the scenarios in which ES is not considered, from those in which the ES contribution is added in the COHERENT CsI and the Dresden-II data set analyses. In the latter case, the different antineutrino fluxes and QFs are also considered.

By comparing Tab. XIII and Tab. XIV, it is clear that the Dresden-II data allow us to significantly reduce the bound on $|\mu_{\nu_e}|$ with respect to COHERENT by more than one order of magnitude. Also in this case, the different antineutrino fluxes result in a negligible difference, while the two QFs produce a much more noticeable effect, with the Fef QF limits being almost a factor of two more precise. Finally, the inclusion of ES results in a marginal improvement of the Dresden-II limits of about 10%. At 90% C.L., the bounds on the neutrino MM obtained in this work are

$$|\mu_{\nu_e}| < 2.13 \times 10^{-10} \mu_B \quad \text{Dresden - II (CE}\nu\text{NS + ES)}, \quad (38)$$

$$|\mu_{\nu_\mu}| < 18 \times 10^{-10} \mu_B \quad \text{CsI (CE}\nu\text{NS + ES) + Ar (CE}\nu\text{NS)}, \quad (39)$$

where for the Dresden-II data the Fef QF has been considered. These limits can be compared with the

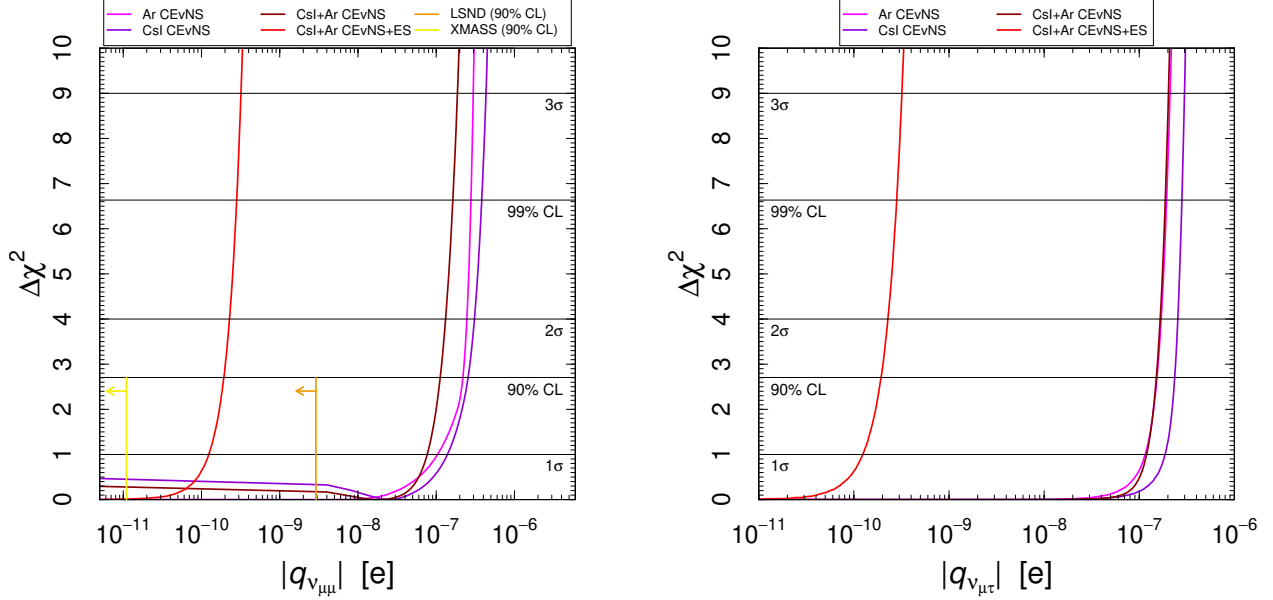


FIG. 10. Marginal $\Delta\chi^2$'s for $|q_{\nu\mu\mu}|$ and $|q_{\nu\mu\tau}|$ obtained from: the separate analyses of the COHERENT Ar (magenta) and CsI (darkviolet) data with CE ν NS interactions; the combined analyses of the COHERENT Ar and CsI data with CE ν NS interactions only (dark red) and with CE ν NS+ES interactions (red). The short vertical orange and yellow lines show the 90% C.L. upper bounds on $|q_{\nu\mu\mu}|$ obtained, respectively, in Ref. [105] from the LSND [96] bound on $|\mu_{\nu\mu}|$ and in the XMASS-I experiment [106] from solar neutrino ES.

bounds obtained in accelerator experiments with $\nu_\mu - e$ scattering (see Table IV of Ref. [67]). The most stringent is the LSND bound $|\mu_{\nu\mu}| < 6.8 \times 10^{-10} \mu_B$ at 90% CL [96], and that on $|\mu_{\nu e}|$ established in reactor neutrino experiments, namely $|\mu_{\nu e}| < 2.9 \times 10^{-11} \mu_B$ [67, 82].

In Fig. 11 we show the marginal $\Delta\chi^2$'s for $|\mu_{\nu e}|$ and $|\mu_{\nu\mu}|$ obtained from the COHERENT Ar and CsI data as well as their combination with the CE ν NS-only analyses of Dresden-II data assuming the HMVE reactor antineutrino flux and the YBe or Fef QF. We also show the impact of the ES contribution assuming the HMVE, HMK, or EFK reactor antineutrino flux and the YBe or Fef QF. For comparison, we also show the 90% C.L. upper bounds on $|\mu_{\nu e}|$ obtained in the MUNU [107], TEXONO [104], and GEMMA [102] experiments; and $|\mu_{\nu\mu}|$ obtained in the BNL-E734 [92], LAMPF [95], and LSND [96] experiments.

Before the completion of this work, other analyses also studying the CE ν NS impact on the neutrino MM appeared on the arXiv [53, 108]. Similar bounds to those found in this work for $|\mu_{\nu e}|$ have been obtained, although with some differences among the various data analyses. Namely, in Ref. [108] a bound at 90% C.L. of $|\mu_{\nu e}| < 2.7 \times 10^{-10} \mu_B$ is found when using a modified Lindahrd model for the QF with $k = 0.157$ and ignoring the ES contribution. Similarly to Ref. [90] only the CE ν NS Dresden-II residuals after the subtraction of the background are fitted, with no background uncertainty propagated in the analysis. In Ref. [53], a bound at 90% C.L. of $|\mu_{\nu e}| < 2.2 \times 10^{-10} \mu_B$ is found when using the Dresden-II data in combination with ES as in this work, also using the Fef QF. In this latter case, a very similar treatment of the Dresden-II data with respect to this work has been followed by the authors, with only minimal differences in the antineutrino flux treatment and least-squares function definition.

V. CONCLUSIONS

In this paper, we describe the results of a combined analysis of all the CE ν NS data set so far available, profiting from the first observation of CE ν NS recently obtained with electron antineutrinos from the Dresden-II reactor site, using the NCC-1701 germanium detector. Thanks to the much lower energy of reactor

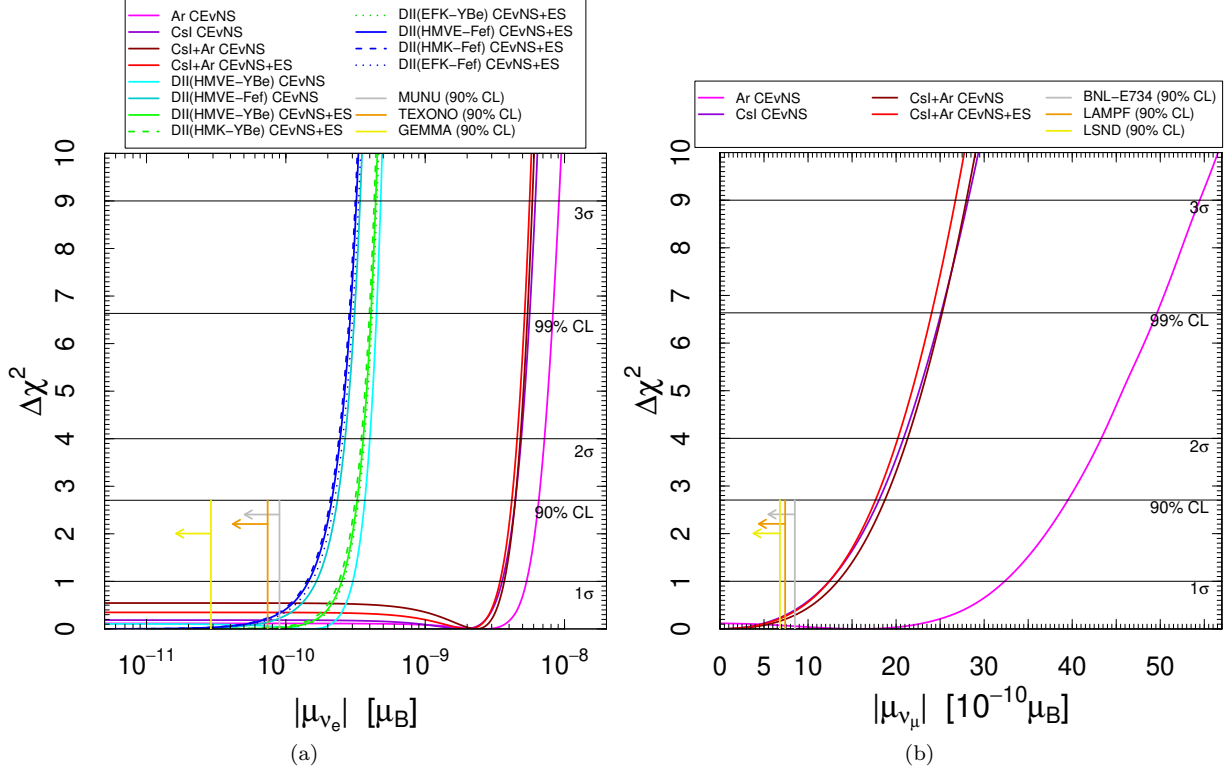


FIG. 11. Marginal $\Delta\chi^2$'s for (a) $|\mu_{\nu_e}|$ and (b) $|\mu_{\nu_\mu}|$ obtained from: the separate analyses of the COHERENT Ar (magenta) and CsI (darkviolet) data with CE ν NS interactions; the combined analyses of the COHERENT Ar and CsI data with CE ν NS interactions only (dark red) and with CE ν NS+ES interactions (red); the CE ν NS-only analyses of Dresden-II data assuming the HMVE reactor antineutrino flux and the YBe (cyan) or Fef (dark cyan) quenching; the CE ν NS+ES analyses of Dresden-II data assuming the HMVE, HMK, or EFK reactor antineutrino flux and the YBe (green) or Fef (blue) quenching. The short vertical gray, orange, and yellow lines show, respectively, the 90% C.L. upper bounds on: (a) $|\mu_{\nu_e}|$ obtained in the MUNU [107], TEXONO [104], and GEMMA [102] experiments; (b) $|\mu_{\nu_\mu}|$ obtained in the BNL-E734 [92], LAMPF [95], and LSND [96] experiments.

antineutrinos and the low energy threshold of semiconductor detectors, these data provide complementary information with respect to CE ν NS processes observed with neutrinos produced at spallation neutron sources, with a negligible dependence on the neutron distribution inside the target nuclei.

Following closely the instructions provided in the various data releases, we analysed the data collected with the CsI and Ar detectors by the COHERENT Collaboration and the recent data set provided by the Dresden-II reactor CE ν NS measurement. We focused in particular on the constraints on electroweak and neutrino electromagnetic properties, namely on the determination of the weak mixing angle and the neutrino magnetic moments, charge radii and millicharges. In the analysis of the Dresden-II reactor data we employ three different antineutrino fluxes, denoted as HMVE, HMK and EFK. We have also studied the dependence of the results on the germanium quenching factor by considering two models: one based on the use of iron-filtered monochromatic neutrons, indicated as Fef, and another one based on photo-neutron source measurements, indicated as YBe. The impact of the various antineutrino fluxes on the results obtained is negligible, while the two quenching factors always result in visible differences in the obtained measurements and limits. This observation clearly underline the necessity of accurate measurements of the germanium quenching factor at low energies. Related to this, during the completion of this work an interesting study appeared [109] in which CE ν NS processes are searched for by the ν GEN Collaboration using antineutrinos from the Kalinin Nuclear Power Plant and a germanium detector. While no CE ν NS excess is observed, assuming the SM the authors set an upper limit on the quenching parameter k of the standard Lindhard

	1σ	90%	2σ	3σ
CsI (CEvNS)				
$ \mu_{\nu_e} $	< 36	< 44	< 49	< 62
$ \mu_{\nu_\mu} $	< 12	< 18	< 21	< 28
CsI (CEvNS+ES)				
$ \mu_{\nu_e} $	< 32	< 41	< 46	< 58
$ \mu_{\nu_\mu} $	< 11	< 17	< 19	< 27
Ar (CEvNS)				
$ \mu_{\nu_e} $	< 53	< 65	< 72	< 91
$ \mu_{\nu_\mu} $	< 32	< 39	< 43	< 54
CsI (CEvNS) + Ar (CEvNS)				
$ \mu_{\nu_e} $	< 37	< 44	< 48	< 59
$ \mu_{\nu_\mu} $	< 13	< 19	< 21	< 28
CsI (CEvNS+ES) + Ar (CEvNS)				
$ \mu_{\nu_e} $	< 34	< 42	< 46	< 56
$ \mu_{\nu_\mu} $	< 12	< 18	< 20	< 27

TABLE XIII. Bounds on the neutrino magnetic moments in units of $10^{-10} \mu_B$ obtained from the analysis of the COHERENT CsI and Ar data. We show the results of the analyses of CsI data with CEvNS only interactions and with CEvNS+ES interactions.

	1σ	90%	2σ	3σ	Interaction
Dresden-II (HMVE-Fef)					
$ \mu_{\nu_e} $	< 1.65	< 2.34	< 2.66	< 3.41	CEvNS
$ \mu_{\nu_e} $	< 1.45	< 2.13	< 2.45	< 3.20	CEvNS+ES
Dresden-II (HMK-Fef)					
$ \mu_{\nu_e} $	< 1.64	< 2.32	< 2.64	< 3.38	CEvNS
$ \mu_{\nu_e} $	< 1.41	< 2.08	< 2.40	< 3.15	CEvNS+ES
Dresden-II (EFK-Fef)					
$ \mu_{\nu_e} $	< 1.79	< 2.49	< 2.81	< 3.57	CEvNS
$ \mu_{\nu_e} $	< 1.54	< 2.23	< 2.56	< 3.32	CEvNS+ES
Dresden-II (HMVE-YBe)					
$ \mu_{\nu_e} $	< 3.02	< 3.68	< 4.00	< 4.79	CEvNS
$ \mu_{\nu_e} $	< 2.51	< 3.25	< 3.58	< 4.41	CEvNS+ES
Dresden-II (HMK-YBe)					
$ \mu_{\nu_e} $	< 2.98	< 3.64	< 3.96	< 4.75	CEvNS
$ \mu_{\nu_e} $	< 2.39	< 3.14	< 3.49	< 4.30	CEvNS+ES
Dresden-II (EFK-YBe)					
$ \mu_{\nu_e} $	< 3.16	< 3.84	< 4.16	< 4.94	CEvNS
$ \mu_{\nu_e} $	< 2.59	< 3.33	< 3.67	< 4.51	CEvNS+ES

TABLE XIV. Bounds on the electron neutrino magnetic moment $|\mu_{\nu_e}|$ in units of $10^{-10} \mu_B$ obtained from the analysis of the Dresden-II data assuming the HMVE, HMK, or EFK reactor antineutrino flux and the Fef or YBe quenching. We show the results obtained with CEvNS only interactions and with CEvNS+ES interactions.

model to be less than 0.177 at 90% confidence level.

Finally, in the analysis of both COHERENT and Dresden-II data, we evaluate the impact of the inclusion of the elastic neutrino-electron scattering contribution. Although in the SM this process contributes in a negligible way to the total event rate at low recoil energies, in certain scenarios beyond the SM the electron scattering contribution could increase significantly, making it important to consider. In particular, given that no electron-recoil discrimination is possible in the CsI and Dresden-II data set, we include the electron scattering contribution in both of them.

From an analysis of the Dresden-II data set alone, we are able to derive a new measurement of the weak mixing angle at low energies. The different antineutrino fluxes have a negligible impact, while the Fef and

YBe quenching factors produce different results, namely

$$\sin^2 \vartheta_W(\text{Dresden} - \text{II Fef}) = 0.219_{-0.05}^{+0.06} (1\sigma),_{-0.08}^{+0.11} (90\%),_{-0.09}^{+0.14} (2\sigma),$$

$$\sin^2 \vartheta_W(\text{Dresden} - \text{II YBe}) = 0.286_{-0.07}^{+0.08} (1\sigma),_{-0.11}^{+0.16} (90\%),_{-0.13}^{+0.22} (2\sigma),$$

focusing thus only on the HMVE flux.

Thanks to a combined Dresden-II and COHERENT analysis, we are able to constrain different neutrino charge radii, namely $\langle r_{\nu ee}^2 \rangle$, $\langle r_{\nu \mu \mu}^2 \rangle$, $|\langle r_{\nu e \mu}^2 \rangle|$, $|\langle r_{\nu e \tau}^2 \rangle|$, and $|\langle r_{\nu \mu \tau}^2 \rangle|$. Assuming the absence of the transition charge radii, we obtain a very competitive limit at 90% C.L. with respect to that set by TEXONO when using the Fef quenching factor, namely

$$-7.1 \times 10^{-32} \text{ cm}^2 < \langle r_{\nu ee}^2 \rangle < 5 \times 10^{-32} \text{ cm}^2.$$

In particular, we are able to restrict the upper bound limit from $6.6 \times 10^{-32} \text{ cm}^2$ to $5 \times 10^{-32} \text{ cm}^2$. No effect due to the inclusion of the electron scattering contribution is observed when fitting for the neutrino charge radii.

Furthermore, we set limits on five neutrino electric charges, namely $q_{\nu ee}$, $q_{\nu \mu \mu}$, $|q_{\nu e \mu}|$, $|q_{\nu e \tau}|$, and $|q_{\nu \mu \tau}|$. In this case, the inclusion of the neutrino-electron scattering allows us to significantly improve the bounds obtained with both COHERENT and Dresden-II data. Thanks to the fact that the $|q|^2$ corresponding to neutrino-electron elastic scattering is much smaller than the CE ν NS $|q|^2$, the inclusion of the ES contribution allows us to achieve more stringent constraints with respect to CE ν NS only. Namely, with CE ν NS only there is an improvement with respect to COHERENT CE ν NS only of about 2 orders of magnitude, while with CE ν NS+ES the improvement is of about 4 orders of magnitude. Intriguingly, the bounds on $q_{\nu ee}$ obtained from the combination of COHERENT with the Dresden-II CE ν NS+ES data set are much more stringent than the COHERENT ones and the CE ν NS only fit, namely at 90% C.L. and using the Fef quenching factor

$$-9.3 \times 10^{-12} e < q_{\nu ee} < 9.5 \times 10^{-12} e.$$

This limit is competitive with respect to the other existing bounds, that are also at the level of $10^{-12} e$.

Finally, we presented the bounds on the neutrino magnetic moments, namely on $|\mu_{\nu e}|$ and $|\mu_{\nu \mu}|$ using the COHERENT data and $|\mu_{\nu e}|$ only using the Dresden-II data. At 90% C.L., the bounds on the neutrino magnetic moments obtained in this work are

$$\begin{aligned} |\mu_{\nu e}| &< 2.13 \times 10^{-10} \mu_B \quad \text{Dresden} - \text{II (CE}\nu\text{NS} + \text{ES)}, \\ |\mu_{\nu \mu}| &< 18 \times 10^{-10} \mu_B \quad \text{CsI (CE}\nu\text{NS} + \text{ES)} + \text{Ar (CE}\nu\text{NS)}, \end{aligned}$$

where for the Dresden-II data the Fef QF has been considered. These limits are still less stringent than the bounds obtained in reactor and accelerator neutrino experiments.

As evident from the results described in this work, the CE ν NS process proved to be once again a spectacular window to test many and diverse sectors, with precision that are competitive to, if not better than, the existing ones. Thus, we strongly encourage all existing and foreseen experimental efforts in this sector, using neutrinos and antineutrinos both from spallation neutron sources and reactor sites.

ACKNOWLEDGMENTS

The work of C. Giunti and C.A. Ternes is supported by the research grant "The Dark Universe: A Synergic Multimessenger Approach" number 2017X7X85K under the program PRIN 2017 funded by the Ministero dell'Istruzione, Università e della Ricerca (MIUR). The work of Y.F. Li and Y.Y. Zhang is supported in part by the National Natural Science Foundation of China under Grant Nos. 12075255, 12075254 and 11835013,

and by the Key Research Program of the Chinese Academy of Sciences under Grant No. XDPB15. The work of Y.Y. Zhang is also supported by China Postdoctoral Science Foundation under Grant No. 2021T140669.

-
- [1] D. Akimov et al. (COHERENT), “Observation of Coherent Elastic Neutrino-Nucleus Scattering,” *Science* **357**, 1123–1126 (2017), arXiv:1708.01294 [nucl-ex].
 - [2] Akimov, D. and others (COHERENT), “COHERENT Collaboration data release from the first observation of coherent elastic neutrino-nucleus scattering,” (2018), arXiv:1804.09459 [nucl-ex].
 - [3] D. Akimov et al. (COHERENT), “First Measurement of Coherent Elastic Neutrino-Nucleus Scattering on Argon,” *Phys. Rev. Lett.* **126**, 012002 (2021), arXiv:2003.10630 [nucl-ex].
 - [4] D. Akimov et al. (COHERENT), “COHERENT Collaboration data release from the first detection of coherent elastic neutrino-nucleus scattering on argon,” (2020), arXiv:2006.12659 [nucl-ex].
 - [5] D. Akimov et al., “Measurement of the Coherent Elastic Neutrino-Nucleus Scattering Cross Section on CsI by COHERENT,” (2021), arXiv:2110.07730 [hep-ex].
 - [6] Daniel Z. Freedman, “Coherent Neutrino Nucleus Scattering as a Probe of the Weak Neutral Current,” *Phys. Rev. D* **9**, 1389–1392 (1974).
 - [7] Pilar Coloma, M. C. Gonzalez-Garcia, Michele Maltoni, and Thomas Schwetz, “COHERENT Enlightenment of the Neutrino Dark Side,” *Phys. Rev. D* **96**, 115007 (2017), arXiv:1708.02899 [hep-ph].
 - [8] Jiajun Liao and Danny Marfatia, “COHERENT constraints on nonstandard neutrino interactions,” *Phys. Lett. B* **775**, 54–57 (2017), arXiv:1708.04255 [hep-ph].
 - [9] Manfred Lindner, Werner Rodejohann, and Xun-Jie Xu, “Coherent Neutrino-Nucleus Scattering and new Neutrino Interactions,” *JHEP* **03**, 097 (2017), arXiv:1612.04150 [hep-ph].
 - [10] C. Giunti, “General COHERENT constraints on neutrino nonstandard interactions,” *Phys. Rev. D* **101**, 035039 (2020), arXiv:1909.00466 [hep-ph].
 - [11] Peter B. Denton, Yasaman Farzan, and Ian M. Shoemaker, “Testing large non-standard neutrino interactions with arbitrary mediator mass after COHERENT data,” *JHEP* **07**, 037 (2018), arXiv:1804.03660 [hep-ph].
 - [12] D. Aristizabal Sierra, Valentina De Romeri, and N. Rojas, “COHERENT analysis of neutrino generalized interactions,” *Phys. Rev. D* **98**, 075018 (2018), arXiv:1806.07424 [hep-ph].
 - [13] H. Bonet et al. (CONUS), “First limits on neutrino electromagnetic properties from the CONUS experiment,” (2022), arXiv:2201.12257 [hep-ex].
 - [14] M. Cadeddu, F. Dordei, C. Giunti, Y. F. Li, E. Picciau, and Y. Y. Zhang, “Physics results from the first COHERENT observation of coherent elastic neutrino-nucleus scattering in argon and their combination with cesium-iodide data,” *Phys. Rev. D* **102**, 015030 (2020), arXiv:2005.01645 [hep-ph].
 - [15] O. G. Miranda, D. K. Papoulias, G. Sanchez Garcia, O. Sanders, M. Tórtola, and J. W. F. Valle, “Implications of the first detection of coherent elastic neutrino-nucleus scattering (CEvNS) with Liquid Argon,” *JHEP* **05**, 130 (2020), [Erratum: *JHEP* **01**, 067 (2021)], arXiv:2003.12050 [hep-ph].
 - [16] M. Cadeddu, N. Cargioli, F. Dordei, C. Giunti, Y. F. Li, E. Picciau, and Y. Y. Zhang, “Constraints on light vector mediators through coherent elastic neutrino nucleus scattering data from COHERENT,” *JHEP* **01**, 116 (2021), arXiv:2008.05022 [hep-ph].
 - [17] M. Cadeddu, N. Cargioli, F. Dordei, C. Giunti, Y. F. Li, E. Picciau, C. A. Ternes, and Y. Y. Zhang, “New insights into nuclear physics and weak mixing angle using electroweak probes,” *Phys. Rev. C* **104**, 065502 (2021), arXiv:2102.06153 [hep-ph].
 - [18] Heerak Banerjee, Bhaskar Dutta, and Sourov Roy, “Probing $L\mu$ - $L\tau$ models with CEvNS: A new look at the combined COHERENT CsI and Ar data,” *Phys. Rev. D* **104**, 015015 (2021), arXiv:2103.10196 [hep-ph].
 - [19] M. Cadeddu, C. Giunti, Y. F. Li, and Y. Y. Zhang, “Average CsI neutron density distribution from COHERENT data,” *Phys. Rev. Lett.* **120**, 072501 (2018), arXiv:1710.02730 [hep-ph].
 - [20] D. K. Papoulias, T. S. Kosmas, R. Sahu, V. K. B. Kota, and M. Hota, “Constraining nuclear physics parameters with current and future COHERENT data,” *Phys. Lett. B* **800**, 135133 (2020), arXiv:1903.03722 [hep-ph].
 - [21] Matteo Cadeddu, Carlo Giunti, Konstantin A. Kouzakov, Yu-Feng Li, Yi-Yu Zhang, and Alexander I. Studenikin, “Neutrino Charge Radii From Coherent Elastic Neutrino-nucleus Scattering,” *Phys. Rev. D* **98**, 113010 (2018), [Erratum: *Phys.Rev.D* **101**, 059902 (2020)], arXiv:1810.05606 [hep-ph].
 - [22] D. K. Papoulias and T. S. Kosmas, “COHERENT constraints to conventional and exotic neutrino physics,” *Phys. Rev. D* **97**, 033003 (2018), arXiv:1711.09773 [hep-ph].
 - [23] M. Cadeddu, F. Dordei, C. Giunti, Y. F. Li, and Y. Y. Zhang, “Neutrino, electroweak, and nuclear physics from COHERENT elastic neutrino-nucleus scattering with refined quenching factor,” *Phys. Rev. D* **101**, 033004 (2020), arXiv:1908.06045 [hep-ph].

- [24] Dimitrios K. Papoulias, “COHERENT constraints after the COHERENT-2020 quenching factor measurement,” *Phys. Rev. D* **102**, 113004 (2020), arXiv:1907.11644 [hep-ph].
- [25] Amir N. Khan and Werner Rodejohann, “New physics from COHERENT data with an improved quenching factor,” *Phys. Rev. D* **100**, 113003 (2019), arXiv:1907.12444 [hep-ph].
- [26] Bhaskar Dutta, Shu Liao, Samiran Sinha, and Louis E. Strigari, “Searching for Beyond the Standard Model Physics with COHERENT Energy and Timing Data,” *Phys. Rev. Lett.* **123**, 061801 (2019), arXiv:1903.10666 [hep-ph].
- [27] Matteo Cadeddu and Francesca Dordei, “Reinterpreting the weak mixing angle from atomic parity violation in view of the Cs neutron rms radius measurement from COHERENT,” *Phys. Rev. D* **99**, 033010 (2019), arXiv:1808.10202 [hep-ph].
- [28] Bhaskar Dutta, Doojin Kim, Shu Liao, Jong-Chul Park, Seodong Shin, and Louis E. Strigari, “Dark matter signals from timing spectra at neutrino experiments,” *Phys. Rev. Lett.* **124**, 121802 (2020), arXiv:1906.10745 [hep-ph].
- [29] Mohammad Abdullah, James B. Dent, Bhaskar Dutta, Gordon L. Kane, Shu Liao, and Louis E. Strigari, “Coherent elastic neutrino nucleus scattering as a probe of a Z' through kinetic and mass mixing effects,” *Phys. Rev. D* **98**, 015005 (2018), arXiv:1803.01224 [hep-ph].
- [30] Shao-Feng Ge and Ian M. Shoemaker, “Constraining Photon Portal Dark Matter with Texono and Coherent Data,” *JHEP* **11**, 066 (2018), arXiv:1710.10889 [hep-ph].
- [31] O. G. Miranda, D. K. Papoulias, O. Sanders, M. Tórtola, and J. W. F. Valle, “Low-energy probes of sterile neutrino transition magnetic moments,” *JHEP* **12**, 191 (2021), arXiv:2109.09545 [hep-ph].
- [32] L. J. Flores, Newton Nath, and Eduardo Peinado, “Non-standard neutrino interactions in U(1)’ model after COHERENT data,” *JHEP* **06**, 045 (2020), arXiv:2002.12342 [hep-ph].
- [33] Alexis Aguilar-Arevalo et al. (CONNIE), “Search for coherent elastic neutrino-nucleus scattering at a nuclear reactor with CONNIE 2019 data,” *JHEP* **05**, 017 (2022), arXiv:2110.13033 [hep-ex].
- [34] H. Bonet et al. (CONUS), “Constraints on Elastic Neutrino Nucleus Scattering in the Fully Coherent Regime from the CONUS Experiment,” *Phys. Rev. Lett.* **126**, 041804 (2021), arXiv:2011.00210 [hep-ex].
- [35] H. Bonet et al. (CONUS), “Novel constraints on neutrino physics beyond the standard model from the CONUS experiment,” *JHEP* **05**, 085 (2022), arXiv:2110.02174 [hep-ph].
- [36] J. Colaresi, J. I. Collar, T. W. Hossbach, C. M. Lewis, and K. M. Yocum, “Suggestive evidence for Coherent Elastic Neutrino-Nucleus Scattering from reactor antineutrinos,” (2022), arXiv:2202.09672 [hep-ex].
- [37] A. Drukier and Leo Stodolsky, “Principles and Applications of a Neutral Current Detector for Neutrino Physics and Astronomy,” *Phys. Rev. D* **30**, 2295 (1984).
- [38] J. Barranco, O. G. Miranda, and T. I. Rashba, “Probing new physics with coherent neutrino scattering off nuclei,” *JHEP* **12**, 021 (2005), arXiv:hep-ph/0508299.
- [39] Kelly Patton, Jonathan Engel, Gail C. McLaughlin, and Nicolas Schunck, “Neutrino-nucleus coherent scattering as a probe of neutron density distributions,” *Phys. Rev. C* **86**, 024612 (2012), arXiv:1207.0693 [nucl-th].
- [40] P. Agnes et al. (DarkSide-20k), “Separating ^{39}Ar from ^{40}Ar by cryogenic distillation with Aria for dark-matter searches,” *Eur. Phys. J. C* **81**, 359 (2021), arXiv:2101.08686 [physics.ins-det].
- [41] Michael Berglund and Michael E. Wieser, “Isotopic compositions of the elements 2009 (iupac technical report),” *Pure and Applied Chemistry* **83**, 397–410 (2011).
- [42] Jens Erler and Shufang Su, “The Weak Neutral Current,” *Prog. Part. Nucl. Phys.* **71**, 119–149 (2013), arXiv:1303.5522 [hep-ph].
- [43] P. A. Zyla et al. (Particle Data Group), “Review of Particle Physics,” *PTEP* **2020 and 2021 update**, 083C01 (2020).
- [44] Richard H. Helm, “Inelastic and Elastic Scattering of 187-Mev Electrons from Selected Even-Even Nuclei,” *Phys. Rev.* **104**, 1466–1475 (1956).
- [45] J. Piekarewicz, A. R. Linero, P. Giuliani, and E. Chicken, “Power of two: Assessing the impact of a second measurement of the weak-charge form factor of ^{208}Pb ,” *Phys. Rev. C* **94**, 034316 (2016), arXiv:1604.07799 [nucl-th].
- [46] Spencer Klein and Joakim Nystrand, “Exclusive vector meson production in relativistic heavy ion collisions,” *Phys. Rev. C* **60**, 014903 (1999), arXiv:hep-ph/9902259.
- [47] G. Fricke, C. Bernhardt, K. Heilig, L. A. Schaller, L. Schellenberg, E. B. Shera, and C. W. de Jager, “Nuclear Ground State Charge Radii from Electromagnetic Interactions,” *Atom. Data Nucl. Data Tabl.* **60**, 177–285 (1995).
- [48] I. Angeli and K. P. Marinova, “Table of experimental nuclear ground state charge radii: An update,” *Atom. Data Nucl. Data Tabl.* **99**, 69–95 (2013).
- [49] G. Fricke and K. Heilig, “Nuclear charge radii · 32-ge germanium: Datasheet from landolt-börnstein - group i elementary particles, nuclei and atoms · volume 20: “nuclear charge radii” in springermaterials (https://doi.org/10.1007/10856314_34),” (2004), copyright 2004 Springer-Verlag Berlin Heidelberg.

- [50] Xu-Run Huang and Lie-Wen Chen, “Neutron Skin in CsI and Low-Energy Effective Weak Mixing Angle from COHERENT Data,” *Phys. Rev. D* **100**, 071301 (2019), arXiv:1902.07625 [hep-ph].
- [51] C. G. Payne, S. Bacca, G. Hagen, W. Jiang, and T. Papenbrock, “Coherent elastic neutrino-nucleus scattering on ^{40}Ar from first principles,” *Phys. Rev. C* **100**, 061304 (2019), arXiv:1908.09739 [nucl-th].
- [52] Martin Hoferichter, Javier Menéndez, and Achim Schwenk, “Coherent elastic neutrino-nucleus scattering: EFT analysis and nuclear responses,” *Phys. Rev. D* **102**, 074018 (2020), arXiv:2007.08529 [hep-ph].
- [53] Pilar Coloma, Ivan Esteban, M. C. Gonzalez-Garcia, Leire Larizgoitia, Francesc Monrabal, and Sergio Palomares-Ruiz, “Bounds on new physics with data of the Dresden-II reactor experiment and COHERENT,” (2022), arXiv:2202.10829 [hep-ph].
- [54] L. A. Mikaelyan, “Investigation of neutrino properties in experiments at nuclear reactors: Present status and prospects,” *Phys. Atom. Nucl.* **65**, 1173–1187 (2002), arXiv:hep-ph/0210047.
- [55] S. A. Fayans, L. A. Mikaelyan, and V. V. Sinev, “Weak and magnetic inelastic scattering of anti-neutrinos on atomic electrons,” *Phys. Atom. Nucl.* **64**, 1475–1480 (2001), arXiv:hep-ph/0004158.
- [56] Konstantin A. Kouzakov and Alexander I. Studenikin, “Theory of neutrino-atom collisions: the history, present status and BSM physics,” *Adv. High Energy Phys.* **2014**, 569409 (2014), arXiv:1406.4999 [hep-ph].
- [57] Konstantin A. Kouzakov and Alexander I. Studenikin, “Electromagnetic properties of massive neutrinos in low-energy elastic neutrino-electron scattering,” *Phys. Rev. D* **95**, 055013 (2017), [Erratum: *Phys. Rev. D* **96**, 099904 (2017)], arXiv:1703.00401 [hep-ph].
- [58] Jiunn-Wei Chen, Hsin-Chang Chi, Keh-Ning Huang, Hau-Bin Li, C. P. Liu, Lakhwinder Singh, Henry T. Wong, Chih-Liang Wu, and Chih-Pan Wu, “Constraining neutrino electromagnetic properties by germanium detectors,” *Phys. Rev. D* **91**, 013005 (2015), arXiv:1411.0574 [hep-ph].
- [59] Chung-Chun Hsieh, Lakhwinder Singh, Chih-Pan Wu, Jiunn-Wei Chen, Hsin-Chang Chi, C.-P. Liu, Mukesh K. Pandey, and Henry T. Wong, “Discovery potential of multiton xenon detectors in neutrino electromagnetic properties,” *Phys. Rev. D* **100**, 073001 (2019).
- [60] A. Thompson et al., “X-ray data booklet, <https://xdb.lbl.gov/>,” (2009).
- [61] K. N. Huang and W. R. Johnson, “Multiconfiguration relativistic random-phase approximation. theory,” *Phys. Rev. A* **25**, 634–649 (1982).
- [62] Keh-Ning Huang, “Relativistic many-body theory of atomic transitions. the relativistic equation-of-motion approach,” *Phys. Rev. A* **26**, 734–739 (1982).
- [63] Jiunn-Wei Chen, Hsin-Chang Chi, Keh-Ning Huang, C. P. Liu, Hao-Tse Shiao, Lakhwinder Singh, Henry T. Wong, Chih-Liang Wu, and Chih-Pan Wu, “Atomic ionization of germanium by neutrinos from an ab initio approach,” *Phys. Lett. B* **731**, 159–162 (2014), arXiv:1311.5294 [hep-ph].
- [64] J. Bernabeu, L. G. Cabral-Rosetti, J. Papavassiliou, and J. Vidal, “On the charge radius of the neutrino,” *Phys. Rev. D* **62**, 113012 (2000), hep-ph/0008114.
- [65] J. Bernabeu, J. Papavassiliou, and J. Vidal, “On the observability of the neutrino charge radius,” *Phys. Rev. Lett.* **89**, 101802 (2002), hep-ph/0206015.
- [66] J. Bernabeu, J. Papavassiliou, and J. Vidal, “The neutrino charge radius is a physical observable,” *Nucl. Phys. B* **680**, 450 (2004), hep-ph/0210055.
- [67] Carlo Giunti and Alexander Studenikin, “Neutrino electromagnetic interactions: a window to new physics,” *Rev. Mod. Phys.* **87**, 531 (2015), arXiv:1403.6344 [hep-ph].
- [68] Carlo Giunti, Konstantin A. Kouzakov, Yu-Feng Li, Alexey V. Lokhov, Alexander I. Studenikin, et al., “Electromagnetic neutrinos in terrestrial experiments and astrophysics,” *Annalen Phys.* **528**, 198–215 (2016), arXiv:1506.05387 [hep-ph].
- [69] M. Atzori Corona, M. Cadeddu, N. Cargioli, F. Dordei, C. Giunti, Y. F. Li, E. Picciau, C. A. Ternes, and Y. Y. Zhang, “Probing light mediators and $(g - 2)_\mu$ through detection of coherent elastic neutrino nucleus scattering at COHERENT,” *JHEP* **05**, 109 (2022), arXiv:2202.11002 [hep-ph].
- [70] D. Akimov et al. (COHERENT), “Measurement of scintillation response of CsI[Na] to low-energy nuclear recoils by COHERENT,” (2021), arXiv:2111.02477 [physics.ins-det].
- [71] Steve Baker and Robert D. Cousins, “Clarification of the Use of Chi Square and Likelihood Functions in Fits to Histograms,” *Nucl. Instrum. Meth.* **221**, 437–442 (1984).
- [72] Th. A. Mueller et al., “Improved Predictions of Reactor Antineutrino Spectra,” *Phys. Rev. C* **83**, 054615 (2011), arXiv:1101.2663 [hep-ex].
- [73] M. Estienne et al., “Updated Summation Model: An Improved Agreement with the Daya Bay Antineutrino Fluxes,” *Phys. Rev. Lett.* **123**, 022502 (2019), arXiv:1904.09358 [nucl-ex].
- [74] P. Vogel and J. Engel, “Neutrino Electromagnetic Form-Factors,” *Phys. Rev. D* **39**, 3378 (1989).
- [75] V. I. Kopeikin, L. A. Mikaelyan, and V. V. Sinev, “Search for the neutrino magnetic moment in the nonequilibrium reactor anti-neutrino energy spectrum,” *Phys. Atom. Nucl.* **63**, 1012–1015 (2000), arXiv:hep-ph/9904384.
- [76] V. I. Kopeikin, “Flux and spectrum of reactor antineutrinos,” *Phys. Atom. Nucl.* **75**, 143–152 (2012).
- [77] J. I. Collar, A. R. L. Kavner, and C. M. Lewis, “Germanium response to sub-keV nuclear recoils: a multipronged

- experimental characterization,” *Phys. Rev. D* **103**, 122003 (2021), arXiv:2102.10089 [nucl-ex].
- [78] J Lindhard, V Nielsen, M Scharff, and P V Thomsen, “Integral equations governing radiation effects. (notes on atomic collisions, iii),” *Kgl. Danske Videnskab., Selskab. Mat. Fys. Medd.* **1804.0945933** (1963).
 - [79] M. Cadeddu, N. Cargioli, F. Dordei, C. Giunti, and E. Picciau, “Muon and electron g-2 and proton and cesium weak charges implications on dark Z_d models,” *Phys. Rev. D* **104**, 011701 (2021), arXiv:2104.03280 [hep-ph].
 - [80] M.S. Safronova, D. Budker, D. DeMille, Derek F. Jackson Kimball, A. Derevianko, and Charles W. Clark, “Search for new physics with atoms and molecules,” *Reviews of Modern Physics* **90** (2018), 10.1103/revmodphys.90.025008.
 - [81] M. Atzori Corona, M. Cadeddu, N. Cargioli, P. Finelli, and M. Vorabbi, “Incorporating the weak mixing angle dependence to reconcile the neutron skin measurement on ²⁰⁸Pb by prex-ii,” *Phys. Rev. C* **105**, 055503 (2022).
 - [82] M. Tanabashi et al. (Particle Data Group), “Review of Particle Physics,” *Phys. Rev.* **D98**, 030001 (2018).
 - [83] Jens Erler and Michael J. Ramsey-Musolf, “The Weak mixing angle at low energies,” *Phys. Rev.* **D72**, 073003 (2005), arXiv:hep-ph/0409169 [hep-ph].
 - [84] Jens Erler and Rodolfo Ferro-Hernández, “Weak Mixing Angle in the Thomson Limit,” *JHEP* **03**, 196 (2018), arXiv:1712.09146 [hep-ph].
 - [85] C. S. Wood, S. C. Bennett, D. Cho, B. P. Masterson, J. L. Roberts, C. E. Tanner, and Carl E. Wieman, “Measurement of parity nonconservation and an anapole moment in cesium,” *Science* **275**, 1759–1763 (1997).
 - [86] V. A. Dzuba, J. C. Berengut, V. V. Flambaum, and B. Roberts, “Revisiting parity non-conservation in cesium,” *Phys. Rev. Lett.* **109**, 203003 (2012), arXiv:1207.5864 [hep-ph].
 - [87] P. L. Anthony et al. (SLAC E158), “Precision measurement of the weak mixing angle in Moller scattering,” *Phys. Rev. Lett.* **95**, 081601 (2005), hep-ex/0504049 [hep-ex].
 - [88] D. Wang et al. (PVDIS), “Measurement of parity violation in electron–quark scattering,” *Nature* **506**, 67–70 (2014).
 - [89] D. Androic et al. (Qweak), “Precision measurement of the weak charge of the proton,” *Nature* **557**, 207–211 (2018).
 - [90] D. Aristizabal Sierra, V. De Romeri, and D. K. Papoulias, “Consequences of the Dresden-II reactor data for the weak mixing angle and new physics,” (2022), arXiv:2203.02414 [hep-ph].
 - [91] M. Deniz et al. (TEXONO), “Measurement of Neutrino-Electron Scattering Cross-Section with a CsI(Tl) Scintillating Crystal Array at the Kuo-Sheng Nuclear Power Reactor,” *Phys. Rev.* **D81**, 072001 (2010), arXiv:0911.1597 [hep-ex].
 - [92] L.A. Ahrens, S.H. Aronson, P.L. Connolly, B.G. Gibbard, M.J. Murtagh, et al., “Determination of electroweak parameters from the elastic scattering of muon-neutrinos and anti-neutrinos on electrons,” *Phys. Rev.* **D41**, 3297–3316 (1990).
 - [93] Martin Hirsch, Enrico Nardi, and Diego Restrepo, “Bounds on the tau and muon neutrino vector and axial vector charge radius,” *Phys. Rev. D* **67**, 033005 (2003), arXiv:hep-ph/0210137.
 - [94] G. S. Vidyakin, V. N. Vyrodov, I. I. Gurevich, Yu. V. Kozlov, V. P. Martemyanov, S. V. Sukhotin, V. G. Tarasenkov, E. V. Turbin, and S. Kh. Khakhimov, “Limitations on the magnetic moment and charge radius of the electron-anti-neutrino,” *JETP Lett.* **55**, 206–210 (1992).
 - [95] R. C. Allen, H. H. Chen, P. J. Doe, R. Hausammann, W. P. Lee, X. Q. Lu, H. J. Mahler, M. E. Potter, K. C. Wang, T. J. Bowles, R. L. Burman, R. D. Carlini, D. R. F. Cochran, J. S. Frank, E. Piasetzky, V. D. Sandberg, D. A. Krakauer, and R. L. Talaga, “Study of electron-neutrino—electron elastic scattering at lampf,” *Phys. Rev. D* **47**, 11–28 (1993).
 - [96] L. B. Auerbach et al. (LSND), “Measurement of electron-neutrino electron elastic scattering,” *Phys. Rev.* **D63**, 112001 (2001), hep-ex/0101039.
 - [97] P. Vilain et al. (CHARM-II), “Experimental study of electromagnetic properties of the muon-neutrino in neutrino - electron scattering,” *Phys. Lett. B* **345**, 115–118 (1995).
 - [98] J. I. Collar, A. R. L. Kavner, and C. M. Lewis, “Response of CsI[Na] to Nuclear Recoils: Impact on Coherent Elastic Neutrino-Nucleus Scattering (CE ν NS),” *Phys. Rev. D* **100**, 033003 (2019), arXiv:1907.04828 [nucl-ex].
 - [99] S. N. Gninenko, N. V. Krasnikov, and A. Rubbia, “Search for millicharged particles in reactor neutrino experiments: A Probe of the PVLAS anomaly,” *Phys. Rev. D* **75**, 075014 (2007), arXiv:hep-ph/0612203.
 - [100] H. B. Li et al. (TEXONO), “Limit on the electron neutrino magnetic moment from the Kuo-Sheng reactor neutrino experiment,” *Phys. Rev. Lett.* **90**, 131802 (2003), arXiv:hep-ex/0212003.
 - [101] Alexander Studenikin, “New bounds on neutrino electric millicharge from limits on neutrino magnetic moment,” *Europhys.Lett.* **107**, 21001 (2014), arXiv:1302.1168 [hep-ph].
 - [102] A.G. Beda, V.B. Brudanin, V.G. Egorov, D.V. Medvedev, V.S. Pogosov, et al., “The results of search for the neutrino magnetic moment in GEMMA experiment,” *Adv.High Energy Phys.* **2012**, 350150 (2012).
 - [103] Jiunn-Wei Chen, Hsin-Chang Chi, Hau-Bin Li, C. P. Liu, Lakhwinder Singh, Henry T. Wong, Chih-Liang Wu, and Chih-Pan Wu (TEXONO), “Constraints on millicharged neutrinos via analysis of data from atomic ionizations with germanium detectors at sub-keV sensitivities,” *Phys. Rev.* **D90**, 011301 (2014), arXiv:1405.7168

- [104] [hep-ph].
- [104] H. T. Wong *et al.* (TEXONO), “A Search of Neutrino Magnetic Moments with a High-Purity Germanium Detector at the Kuo-Sheng Nuclear Power Station,” *Phys. Rev. D* **75**, 012001 (2007), arXiv:hep-ex/0605006.
- [105] Arindam Das, Diptimoy Ghosh, Carlo Giunti, and Arun Thalappilil, “Neutrino charge constraints from scattering to the weak gravity conjecture to neutron stars,” *Phys. Rev. D* **102**, 115009 (2020), arXiv:2005.12304 [hep-ph].
- [106] K. Abe *et al.* (XMASS), “Search for exotic neutrino-electron interactions using solar neutrinos in XMASS-I,” *Phys. Lett. B* **809**, 135741 (2020), arXiv:2005.11891 [hep-ex].
- [107] Z. Daraktchieva *et al.* (MUNU), “Final results on the neutrino magnetic moment from the MUNU experiment,” *Phys. Lett. B* **615**, 153–159 (2005), arXiv:hep-ex/0502037.
- [108] Jiajun Liao, Hongkai Liu, and Danny Marfatia, “Implications of the first evidence for coherent elastic scattering of reactor neutrinos,” (2022), arXiv:2202.10622 [hep-ph].
- [109] I. Alekseev *et al.* (nuGeN), “First results of the nuGeN experiment on coherent elastic neutrino-nucleus scattering,” (2022), arXiv:2205.04305 [nucl-ex].